J. Fluid Mech. (1977), *vol.* 79, *part* 1, *pp.* 1–31
Printed in Great Britain

Numerical solutions of single-mode convection equations

By JURI TOOMRE,

Joint Institute for Laboratory Astrophysics and Department of Astro-Geophysics, University of Colorado, Boulder

D. O. GOUGH

Institute of Astronomy and Department of Applied Mathematics and Theoretical Physics, University of Cambridge

AND E. A. SPIEGEL

Astronomy Department, Columbia University, New York 10027

(Received 1 October 1975)

Truncated modal equations have been proposed (Gough, Spiegel & Toomre 1975*a*) as a means of describing thermal convection. In the Boussinesq approximation these nonlinear modal equations are constructed by expanding the fluctuating velocity and temperature fields in a complete set of functions (or planforms) of the horizontal co-ordinates, and then truncating the expansion. The severest truncation retains but one and yields the 'single-mode equations'. Within this description the convection has a simple cellular structure with a prescribed horizontal planform and an associated horizontal wavenumber a. For most planforms the single-mode equations contain inertia terms and hence the Prandtl number.

In this paper we report numerical solutions of the single-mode equations, considering mostly hexagonal planforms. Extensive surveys of steady solutions are presented here for various Rayleigh numbers R, Prandtl numbers σ and horizontal wavenumbers a. The dependences on R and σ at very large R are in satisfactory agreement with the results of asymptotic expansions.

The wavenumber a is a parameter in this treatment and there is no accepted theoretical reason for clearly preferring any particular value. Reference is made to available laboratory experiments on convection in seeking guidance in choosing a. Solutions at two values of a (for given R and σ) can replicate the experimental heat transport; the lesser value of a, lying below the wavenumber that maximizes the heat transport, seems preferred since the mean temperature profile then has a nearly isothermal interior, not unlike the experimental profiles. This wavenumber increases with increasing R. The asymmetric mean temperature profiles (for hexagons) and the fluctuating temperature and velocity fields of the single-mode solutions are compared with available experimental data, and qualitative agreement is found at moderate Rayleigh numbers.

1. Introduction

In a recent paper (Gough *et al.* 1975*a*, herein referred to as I) we discussed an approximation procedure for computing the mean quantities relating to thermal convection. The procedure is to decompose the spatially fluctuating part of the temperature and the velocity in the horizontal planform functions of linear theory. This leads to a system of equations for the amplitude functions of the expansion, which generally depend only on the vertical co-ordinate and time. The question that we posed was how well can one represent the gross features of thermal convection if we retain only a very few terms in the expansion?

Some aspects of the results obtained to date seem to provide a fairly satisfactory representation of the heat transfer and mean temperature observed in laboratory experiments. These quantities depend explicitly on the vertical structure of the solution. Though the vertical structure is in turn intimately linked to the full spatial complexities of the motion, it appears that for some purposes it is possible to be inaccurate with the horizontal structure of the solution provided that careful attention is paid to the vertical structure.

We carried this notion to its extreme in I and retained only one term in the expansion. We found in some preliminary numerical integrations of the resulting nonlinear partial differential equations that the solutions always tended to steady states as they evolved in time. So we restricted ourselves to studying the steady equations, which had already been found in another way by Roberts (1966). Our main aim was to look in detail at the behaviour of the solutions at very large Rayleigh number. This asymptotic behaviour will be summarized briefly in § 3. What interests us here, though, is the extent to which solutions of this single-mode truncation may approximate experimental results. To discuss this in any detail we need more than the asymptotic results since the experiments do not extend to the very high Rayleigh numbers at which the solutions become asymptotic. Therefore we present here numerical solutions of the single-mode equations for a wide range of the relevant parameters and compare some of their properties with the asymptotic solutions (which provides a check) and with the available experimental results. We find that the observed dependence of the gross properties of convection on the governing parameters is tolerably represented. But this perhaps puts the matter too favourably since if we retain just one term in the expansion we must choose the planform rather arbitrarily.

In the single-mode equations the chosen planform is represented by two parameters: a, the horizontal wavenumber, and C, an indicator of the horizontal structure. We have then two parameters at our disposal to help us fit the data. Our main difficulty is that the experimental results are not extensive enough to guide us in the choice of a and C for a wide enough range of the governing parameters. This difficulty hampers us in the ultimate purpose of this investigation, which we should recall at this point.

Our aim is not to provide a basic theory but rather to find a scheme which will permit us to compute convective heat transfer, and perhaps such additional quantities as time scales and amplitudes of motion. The principal example we

have in mind is stellar convection, for which the parameters are not accessible to laboratory simulation. There one needs an algorithm for computing mean quantities, and direct tests of the results are not readily found. Hence we feel that only a scheme that has demonstrated its usefulness for laboratory convection can be considered adequate.

We might add, though, that in the lowest approximation this expansion procedure seems to provide systems which have the mathematical flavour of the full convection problem. The extent to which this is true becomes clearer in two- and three-mode systems, which display time dependences reminiscent of actual convection; we plan to report on this in a later paper. Here we confine ourselves to the question: is there some modest level of truncation which gives reasonable heat transport in highly unstable configurations?

2. Equations

We consider, as in I, a fluid in the Boussinesq approximation bounded by two infinite horizontal plates maintained at constant temperatures. The fluid temperature T, which is measured in units of the temperature difference ΔT between the plates, is decomposed into mean and fluctuating parts: $T = \overline{T} + \theta$, where the overbar denotes horizontal average. Length and time are measured in units of the plate separation d and d^2/κ, where κ is the thermometric conductivity, and all variables here are dimensionless.

In I the velocity $\mathbf{u}$ and the temperature fluctuation θ were expanded in terms of a complete set of functions of the horizontal co-ordinates. In the single-mode approximation just one term in the expansion is retained. The velocity was written as

$$\mathbf{u} = \left(a^{-2}\frac{\partial W}{\partial z}\frac{\partial f}{\partial x}, a^{-2}\frac{\partial W}{\partial z}\frac{\partial f}{\partial y}, Wf\right), \tag{2.1}$$

which satisfies the continuity equation, and the temperature fluctuation takes the form

$$\theta = \Theta f. \tag{2.2}$$

We note that a possible vertical vorticity term has been suppressed. The amplitude functions W and Θ depend on z and t alone, and the horizontal planform $f(x, y)$ satisfies

$$\partial^2 f/\partial x^2 + \partial^2 f/\partial y^2 = -a^2 f, \quad \overline{f^2} = 1. \tag{2.3}$$

Here t is time, (x, y, z) are spatial Cartesian co-ordinates with z vertical, and a is a horizontal wavenumber. These forms for $\mathbf{u}$ and θ are substituted into the equations of motion, which are subsequently horizontally averaged, or multiplied by f and then averaged. The resulting equations, after elimination of pressure and horizontal velocity components, are

$$\left(\frac{1}{\sigma}\frac{\partial}{\partial t} - \mathscr{D}\right)\mathscr{D}W + Ra^2\Theta = -\frac{C}{\sigma}\left(2\frac{\partial W}{\partial z}\mathscr{D}W + W\mathscr{D}\frac{\partial W}{\partial z}\right), \tag{2.4}$$

$$\left(\frac{\partial}{\partial t} - \mathscr{D}\right)\Theta + \frac{\partial \overline{T}}{\partial z}W = -C\left(2W\frac{\partial \Theta}{\partial z} + \Theta\frac{\partial W}{\partial z}\right), \tag{2.5}$$

and
$$\left(\frac{\partial}{\partial t}-\frac{\partial^2}{\partial z^2}\right)\overline{T} = -\frac{\partial}{\partial z}(W\Theta), \tag{2.6}$$

where $\mathscr{D} \equiv (\partial^2/\partial z^2 - a^2)$ and $C = \frac{1}{2}\overline{f^3}$. Also $R = g\alpha\Delta T d^3/\kappa\nu$ and $\sigma = \nu/\kappa$ are the Rayleigh and Prandtl numbers, where g is the gravitational acceleration, α is the coefficient of thermal expansion and ν is the kinematic viscosity. These quantities, together with κ, have all been assumed constant. Setting the self-interaction parameter C to zero reduces the equations to what are sometimes called the 'single-α mean-field equations'. The single-mode representation of rolls and rectangles has no self-interaction ($C = 0$), but a hexagonal planform has $C = 6^{-\frac{1}{2}} = 0{\cdot}408$, which value we shall use extensively.

When the solutions are steady, $\partial/\partial t = 0$ and the mean thermal energy equation (2.6) has a first integral

$$-d\overline{T}/dz + W\Theta = N. \tag{2.7}$$

The constant of integration N is the Nusselt number.

We assume that the boundaries are perfect thermal conductors, with the constant imposed boundary temperatures

$$T = \overline{T} = 1 \quad \text{at} \quad z = 0, \quad T = \overline{T} = 0 \quad \text{at} \quad z = 1. \tag{2.8}$$

The conditions $\mathbf{u} = 0$ and $\theta = 0$ at rigid boundaries are represented by

$$W = \partial W/\partial z = \Theta = 0 \quad \text{at} \quad z = 0, 1. \tag{2.9}$$

When the horizontal viscous stresses are presumed zero, as for so-called 'free' boundaries, the conditions are

$$W = \partial^2 W/\partial z^2 = \Theta = 0 \quad \text{at} \quad z = 0, 1. \tag{2.10}$$

Equations (2.4)–(2.6) admit the same static solutions as do the full Boussinesq equations, and their linear version corresponds to the usual normal-mode analysis of convective stability theory (Chandrasekhar 1961, chap. 2). Steady nonlinear solutions bifurcate from the marginally stable solutions of linear theory, and in I we considered only those which bifurcate from the gravest modes. In these solutions $W(z)$ has no zeros away from the boundaries; solutions bifurcating from higher modes exist and we shall display one, but in general we are concerned only with the gravest solutions.

A useful property of the steady solutions follows from a symmetry of the equations (Roberts 1966), which, in the steady case, are invariant under the transformation

$$z \to 1-z, \quad W \to -W, \quad \Theta \to -\Theta, \quad \overline{T} \to 1-\overline{T}. \tag{2.11}$$

Thus if one solution is known, a second solution with the same Nusselt number may be generated from it, unless $C = 0$, when the same solution (apart from a horizontal translation) is generated. In the case of hexagons the two solutions correspond to upward and downward motion in the centre of the cell.

The steady equations are also invariant under the transformation $z \to 1-z$, $C \to -C$, $\overline{T} \to 1-\overline{T}$, $W \to W$, $\Theta \to \Theta$. This provides no new information and we shall consider only $C > 0$. For the gravest solutions W has only one sign throughout, and we take the solution with $W > 0$.

In I steady asymptotic solutions of the above equations at large values of the Rayleigh number were derived. The principal results are summarized in the next section.

3. Summary of asymptotic properties at large R

In I we discussed steady single-mode solutions in the limit of large R using matched asymptotic expansions. Throughout most of this paper we shall deal only with solutions satisfying rigid boundary conditions (2.9), and we summarize here asymptotic results pertaining to these conditions. When C, a and σ are all of order unity we found

$$N \sim \mathring{k}^{-1} [\tfrac{3}{5} \mathscr{R} \ln \mathscr{R}]^{\frac{1}{3}} \left[1 - \frac{7}{15} \frac{\ln \ln \mathscr{R}}{\ln \mathscr{R}} + \ldots\right] \quad \text{as} \quad \mathscr{R} \to \infty, \tag{3.1}$$

where

$$\mathscr{R} = Ra^2\sigma/\mathring{k}C$$

and

$$\mathring{k} = k + \mathscr{R}^{-\frac{1}{25}} (\tfrac{3}{5} \ln \mathscr{R})^{\frac{4}{25}} k';$$

k and k' are functions of σ and C, and k is tabulated in I. When $\sigma \gg 1$, $k \propto (\sigma/C)^{\frac{1}{3}}$, with a coefficient which varies weakly with C and is approximately 1·60 when $C = 6^{-\frac{1}{2}}$; hence for $\sigma \gg 1$, N depends very weakly on σ. When $\sigma \ll 1$, $k \simeq 1{\cdot}06\ (1 + C^2)^{\frac{1}{2}}$.

The velocity amplitude $W(z)$ has a single maximum in the interior proportional to

$$\epsilon^{-1} \sim [\mathscr{R}\ (\tfrac{3}{5} \ln \mathscr{R})^{\frac{1}{3}}]^{\frac{2}{3}} \left[1 - \frac{7}{45} \frac{\ln \ln \mathscr{R}}{\ln \mathscr{R}} + \ldots\right]; \tag{3.2}$$

the constant of proportionality depends on a alone but was not explicitly determined in I. The thickness of the lower boundary layer (when $C > 0$) is of order

$$\delta_1 \sim \epsilon^{\frac{1}{2}} \lambda^{-\frac{1}{6}} \sim \mathrm{N}^{-1}, \tag{3.3}$$

where $\lambda = \frac{3}{2} \ln (1/\epsilon)$. Within this boundary layer the mean temperature drops from unity to approximately $\overline{T}_i$, its value in the asymptotically isothermal interior, with

$$\overline{T}_i/(1 - \overline{T}_i) \simeq \mathscr{R}^{-\frac{1}{25}} (\tfrac{3}{5} \ln \mathscr{R})^{\frac{4}{25}} k'/k. \tag{3.4}$$

Also

$$\overline{T}_i \sim \delta_2 N \sim \epsilon^{\frac{1}{10}} \lambda^{\frac{1}{6}}, \tag{3.5}$$

where $\delta_2 \sim \epsilon^{\frac{3}{5}}$ is the thickness of the upper boundary layer, so that $-d\overline{T}/dz \sim N$ as the upper boundary is approached. The mean temperature is not exactly constant in the interior, but has a small negative curvature of order $\epsilon^{\frac{1}{2}} \lambda^{\frac{1}{3}}$. This leads to a bump in $\overline{T}$ in the lower boundary layer whose depth is approximately 0·1 as $R \to \infty$.

As $C \to 0$ this analysis is no longer valid but a separate study for $C = 0$ and $a = O(1)$ (Stewartson 1966; see also Roberts 1966) shows that N is independent of the Prandtl number σ, and asymptotically

$$N \sim 0{\cdot}278\ (Ra^2 \ln Ra^2)^{\frac{1}{3}} \quad \text{as} \quad R \to \infty. \tag{3.6}$$

These results hold provided that a is of order unity. As $a \to R^{-\frac{1}{2}}$ or $a \to R^{\frac{1}{4}}$, (3.6) no longer holds since marginal stability is approached and $N \to 1$. However, when a and N are large the limit (3.1) must be modified to become

$$N \sim k^{-1}\left(1-\frac{a^4}{R}\right)\left[\frac{3(1-3\gamma)}{5(1+2\gamma)}\left(1-\frac{a^4}{R}\right)\tilde{\mathscr{R}}\ln\tilde{\mathscr{R}}\right]^{\frac{1}{5}} \times\left[1-\frac{7(1+2\gamma)}{15(1-3\gamma)}\frac{\ln\ln\tilde{\mathscr{R}}}{\ln\tilde{\mathscr{R}}}+\ldots\right] \quad \text{as} \quad \tilde{\mathscr{R}}\to\infty, \tag{3.7}$$

where $\tilde{\mathscr{R}} = (1-a^4/R)\,\mathscr{R}$ and $\gamma = \ln a/\ln R$. Similar modifications must be made to the limit (3.6) (Stewartson 1966). These modifications are valid provided that $a \ll R^{\frac{4}{17}}(\ln R)^{\frac{2}{51}}$; when a is even larger minor additional ammendments should be made to account for the contributions to N from intermediate boundary layers. With these modifications the asymptotic forms for N, for both $C = 0$ and C of order unity, achieve maxima with respect to a, with N_m proportional to $R^{\frac{3}{10}}(\ln R)^{\frac{1}{5}}$, at $a = a_m = (\frac{1}{13}R)^{\frac{1}{4}}$, as $R \to \infty$. For these large values of a, the amplitudes W and Θ are asymptotically constant in the interior, and $\bar{T}_i$ is no longer constant.

When $C \neq 0$, N decreases when σ does. If $\sigma \ll 1$, N depends on σ, R and C only in the combination $\sigma R/C$. The limit (3.1) holds provided $N \gg 1$ (i.e. $\sigma \gg CR^{-1}$), but when $\sigma \ll CR^{-1}$,

$$N \sim 1+\Lambda\,(\sigma R/C)^2, \tag{3.8}$$

where Λ is a function of a alone; it has a single maximum, $\Lambda_m = 2{\cdot}496\times10^{-6}$, at $a = a_m = 2{\cdot}370$. In this limit, most of the heat is transported by conduction and thermal boundary layers are no longer present, but extremely thin viscous boundary layers ($\delta_1 \sim R^{-\frac{1}{2}}$, $\delta_2 \sim R^{-\frac{3}{8}}$) do exist.

4. Survey of numerical solutions

We have obtained numerical solutions of the single-mode equations by procedures described in appendix A. As mentioned there, solutions of these equations always eventually became time independent, and thus only steady solutions are presented here. Further, all results unless specifically stated otherwise are for the rigid boundary conditions (2.9).

A typical solution at moderate Rayleigh number with $C = 6^{-\frac{1}{2}}$ and $a = 1$ is illustrated in figure 1. It is similar to the solutions with $C = 0$ computed by Herring (1964). The vertical-velocity amplitude is smooth and has a single maximum. In the interior most of the heat is transported by convection since $d\bar{T}/dz$ is small and $W\Theta \simeq N$ [cf. (2.7)]. Thus $\Theta \propto W^{-1}$, and deviations from this behaviour occur only in the boundary layers, where Θ turns over and finally drops to zero, and where thermal conduction is important. The mean temperature gradient becomes comparable with $W\Theta$ at the peak in Θ, while it reaches its maximum magnitude of N at the boundaries, where the convective heat flux vanishes. The negative curvature of the interior mean temperature predicted by the asymptotic analysis for $R \to \infty$ is evident, the asymmetry of $\bar{T}$ following

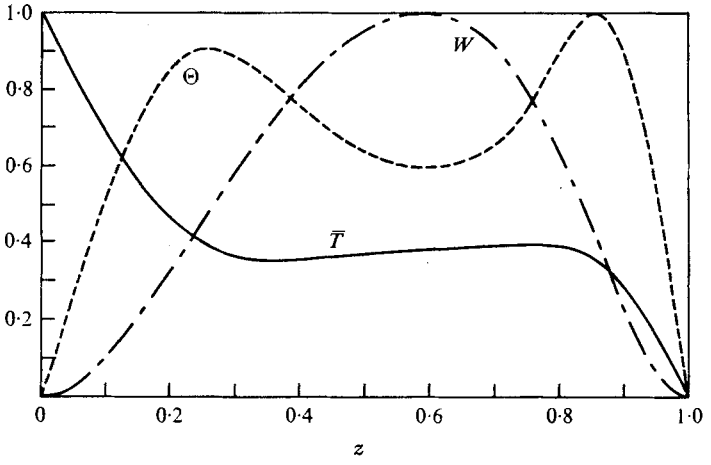

FIGURE 1. A typical steady single-mode solution at moderate Rayleigh number. The amplitude functions W (vertical velocity) and Θ (fluctuating temperature) and the mean temperature $\bar{T}$ are displayed as functions of the vertical co-ordinate z. Here $R = 10^5$, $a = 1$, $C = 6^{-\frac{1}{2}}$ and $\sigma = 1$; the Nusselt number $N = 3{\cdot}2$. The functions W and Θ are plotted in units of their maximum values $W_0 = 26{\cdot}8$ and $\Theta_0 = 0{\cdot}204$. This solution, like most others in this paper, satisfies the rigid boundary conditions (2.9).

that of Θ (see also figure 3). With this general appearance of the solutions in mind, we now discuss how various features of the solutions depend on the parameters a, R, C and σ in turn.

4.1. *Dependence on wavenumber a*

Figure 2 shows the variation of $N-1$ with a for $\sigma = 1$, $C = 6^{-\frac{1}{2}}$ and for different values of R. For each R the Nusselt number has a single maximum N_m at $a = a_m(R)$, and N approaches unity as a approaches its two marginally stable values. If a is not between these values, no non-trivial solutions are found. In the range for which we computed a_m ($10^6 \leqslant R \leqslant 10^{15}$), its value increases with R very slightly faster than $R^{\frac{1}{3}}$ and is $0{\cdot}44\,R^{\frac{1}{3}}$ at $R = 10^{15}$. Similar results hold when $C = 0$ (cf. Herring 1964), at least for moderate R. This can be seen in figure 7, which illustrates the effect of varying C on the dependence of N on a.

Velocity and temperature fields at $R = 10^6$ and $\sigma = 1$ for $a = 2$, 12 and 24 are shown in figure 3. The first and third of these solutions have the same Nusselt number, $N = 7{\cdot}9$, while the second is for $a = 12 \approx a_m$, when $N = 13{\cdot}1$. It is evident from figures 3(a) and (b) that as a increases the position of the maximum of W moves upwards; according to the analysis for large R in appendix B of I, this maximum occurs in a boundary layer of thickness $\sim a^{-1}$ when $a \gg 1$. The solution with the largest wavenumber has W and Θ almost constant in the interior. This property is a consequence of a being so large that buoyancy is balanced by viscous forces in the interior, and is characteristic of all solutions with $\sigma = O(1)$ and $a \gg R^{\frac{1}{3}}$ (when $R^{\frac{1}{3}} \gg 1$). Another prominent feature of the solution with $a = 24$ is that, in contrast to the solutions with

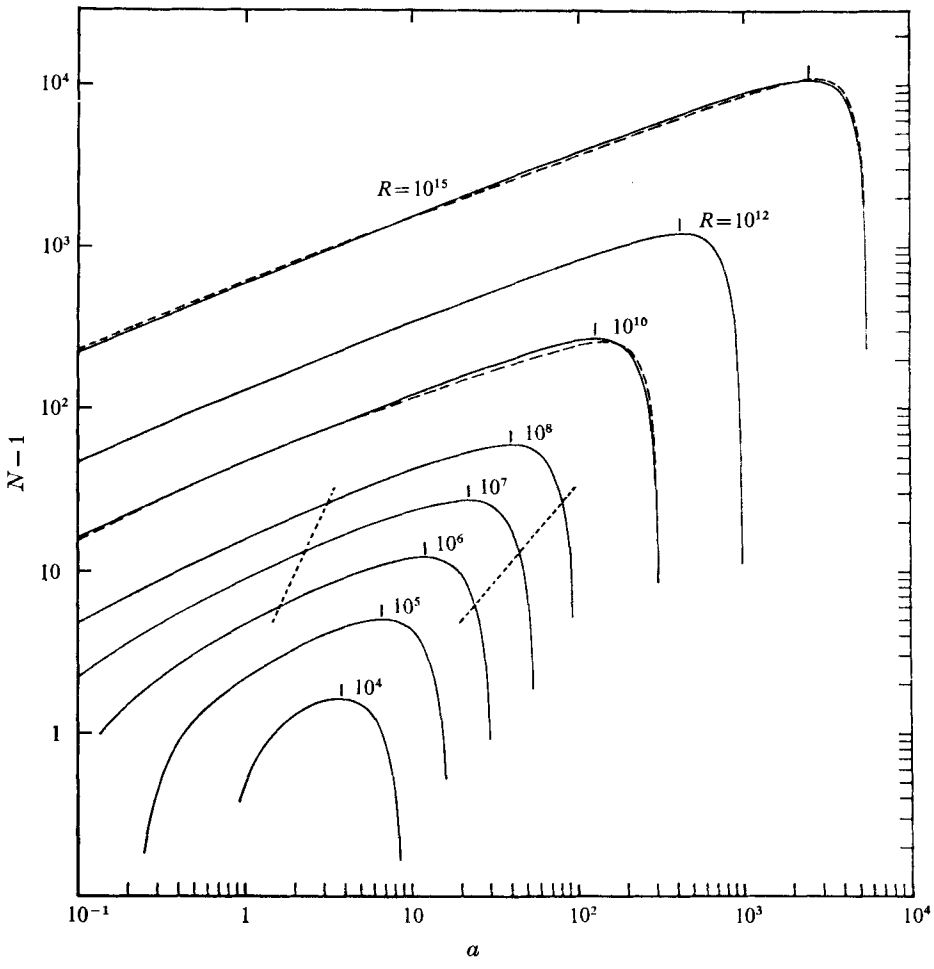

FIGURE 2. The variation of the Nusselt number N with horizontal wavenumber a for the single-mode solutions is shown for various fixed Rayleigh numbers R, all at $\sigma = 1$ and $C = 6^{-\frac{1}{2}}$. For each R the function $N-1$ has a single maximum at $a = a_m$, indicated by a tick mark. $N-1$ vanishes as a approaches either of its marginally stable values, which are $O(R^{-\frac{1}{4}})$ and $O(R^{\frac{1}{2}})$ as $R \to \infty$. The dotted lines indicate which of these solutions (at any given R there are two) replicate the values of N measured by Goldstein & Chu (1971) in experiments with air ($\sigma = 0{\cdot}7$). The dashed curves accompanying the $R = 10^{10}$ and 10^{15} numerical solutions are obtained from the asymptotic formula (3.7).

$a = 2$ and 12, the interior is not isothermal. Indeed, when $R \to \infty$ and $N/N_m \ll 1$ with $a > a_m$, nearly all the drop in the mean temperature across the layer occurs in the interior.

4.2. *Dependence on Rayleigh number R*

The dependence of $N-1$ on R for $\sigma = 1$ and various values of a is shown in figures 4(a) and (b). Most of the curves are for hexagons with rigid boundaries but we include also one case of a hexagon with free boundaries and one roll

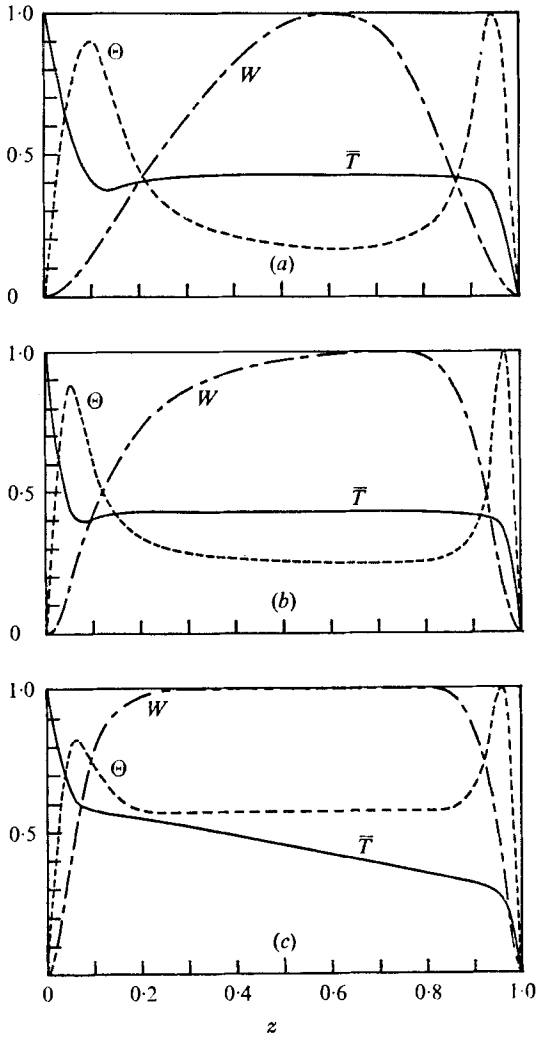

FIGURE 3. These solutions illustrate the behaviour of the fields as the wavenumber a is varied. Each panel displays W, Θ and $\overline{T}$ as functions of z, with W and Θ measured in units of their maximum values W_0 and Θ_0. The three solutions have $a = 2$, 12 and 24, and all are for $R = 10^6$, $C = 6^{-\frac{1}{2}}$ and $\sigma = 6{\cdot}8$ (water). Two of the wavenumbers ($a = 2$ and 24) were chosen to display two solutions whose common value of the Nusselt number ($N = 7{\cdot}9$) is close to that reported in laboratory experiments, while the solution at the intermediate wavenumber $a = 12$ is the one that maximizes the heat transport (with $N = 13{\cdot}1$). (*a*) $W_0 = 249$, $\Theta_0 = 0{\cdot}184$, $a = 2$. (*b*) $W_0 = 299$, $\Theta_0 = 0{\cdot}178$, $a = 12$. (*c*) $W_0 = 115$, $\Theta_0 = 0{\cdot}116$, $a = 24$.

solution with rigid boundaries. The trend is the same for all curves: N increases with R.

We note that in general the curves (which are on logarithmic scales) have slight negative curvatures, which indicates that N is not a simple power of R for fixed a. This is to be expected from the asymptotic results, which show that a transcendental function enters the relation between N and R for $a = O(1)$

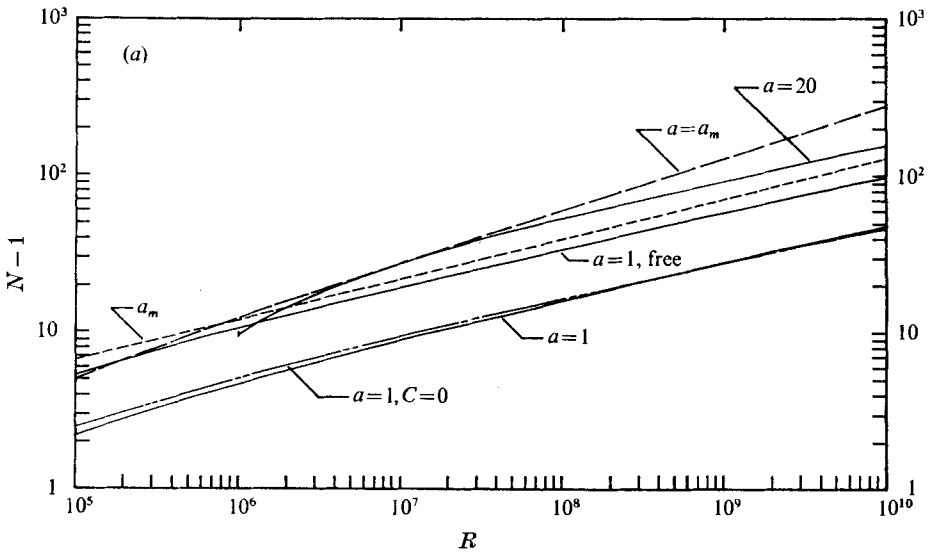

FIGURE 4. For caption to above see p. 11.

and that further complications enter when a is sufficiently small or large. The termini at low R of the curves for high a occur where we ceased the surveys.

The envelope of the curves $N-1$ *vs.* R as a varies is also shown in figure 4; it is simply $N_m(R)-1$. Many more solutions than are explicitly displayed in figures 2 and 4 were used to compute this envelope. It too has a slight negative curvature, as the logarithms in the asymptotic formula for N imply. Each curve in figure 4 touches the envelope when (and if) R passes through that value for which $a = a_m$.

For purposes of comparison, the dependences of $N-1$ upon R at $a = 1$ with $C = 0$ and rigid boundary conditions and with $C = 6^{-\frac{1}{2}}$ and free boundary conditions are also shown in figure 4. The Nusselt number for the flow with free boundary conditions is greater than that for the corresponding flow with rigid boundaries throughout the range of computation. According to the analysis in I, this is true also as $R \to \infty$. The Nusselt number for $C = 6^{-\frac{1}{2}}$ exceeds that for the corresponding solution with $C = 0$ at large R, in accord with the asymptotic analysis, but the curves cross at a Rayleigh number of about 2×10^9. More detailed discussion of the dependence of N upon C is deferred until the following subsection.

Typical velocity and temperature fields are displayed in figures 5 and 6 for various Rayleigh numbers. Because the thermal boundary layers become very thin as R increases, it is convenient to plot them with respect to a stretched co-ordinate ξ to make their structure visible. The independent variable z is also shown, and gives some idea of the degree of stretching in the boundary layers. The most obvious trends, apart from changes in scale, are the development of an extensive isothermal interior and the decrease in both the interior mean temperature and the temperature fluctuation in the upper boundary layer as R increases. The $\overline{T}$ bump in the lower boundary layer is barely evident at

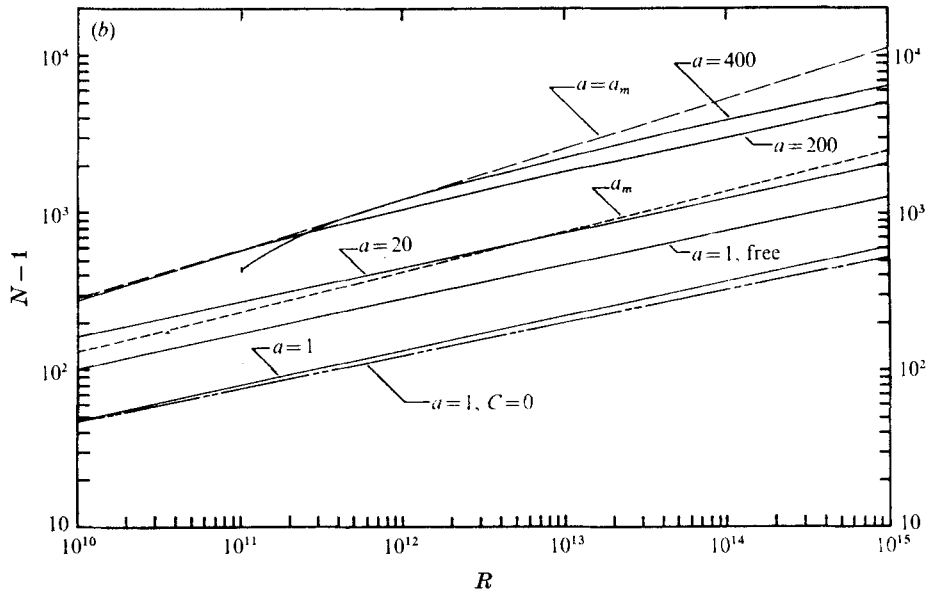

FIGURE 4. Variation of heat transport $N-1$ with Rayleigh number R over (a) the range 10^5–10^{10} and (b) the range 10^{10}–10^{15} for a variety of circumstances. Each curve represents solutions at the fixed value of the wavenumber a indicated, except for the curve labelled $a = a_m$, which gives the maximum of $N-1$ with respect to a. The curve marked a_m shows the value a_m of the wavenumber at which that maximum occurs. All curves are for $\sigma = 1$, and all solutions satisfy rigid boundary conditions (2.9) except those labelled 'free', which satisfy conditions (2.10). All solutions are for $C = 6^{-\frac{1}{2}}$ except those labelled $C = 0$.

$R = 10^5$. Also typical of large R are the two maxima in Θ. If R is decreased sufficiently the $\overline{T}$ bump disappears, the two maxima in Θ coalesce and the solutions approach the linear modes at marginal stability.

The difference between the temperature at the bottom of the $\overline{T}$ bump and that of the isothermal interior increases with R, and according to the asymptotic analysis tends to a finite value of about 0·1 as $R \to \infty$. Since the interior mean temperature tends to zero as $R \to \infty$, this implies that $\overline{T}$ eventually leaves the range defined by the boundary conditions, doing so for $R \gtrsim 10^{30}$. This was raised as an issue of some concern in I. At a given value of z, the total temperature in hexagonal flows varies in the horizontal between $\overline{T} - (\frac{3}{2})^{\frac{1}{2}}\Theta$ and $\overline{T} + 6^{\frac{1}{2}}\Theta$; we find for example that $\overline{T} - (\frac{3}{2})^{\frac{1}{2}}\Theta$ is negative at some z for $R \gtrsim 10^{12}$ when $a = 1$ or 200, and for $R \gtrsim 10^8$ when $a = 20$. This feature of the single-mode equations for $C \neq 0$ seems totally unphysical and indicates the need to include more modes at large R. Nevertheless, it does not seem to produce unreasonable values of N.

Typical fields for $C = 0$ at moderate R are provided by Herring (1964) for rigid boundary conditions. Where comparison is possible they agree with our results for $C = 0$ to within 1 or 2 %. However, the solutions at relatively low R for $C = 6^{\frac{1}{2}}$ published by Roberts (1966) differ somewhat from ours. [For free boundary conditions Herring (1963) and Murphy (1971*a*) have given solutions

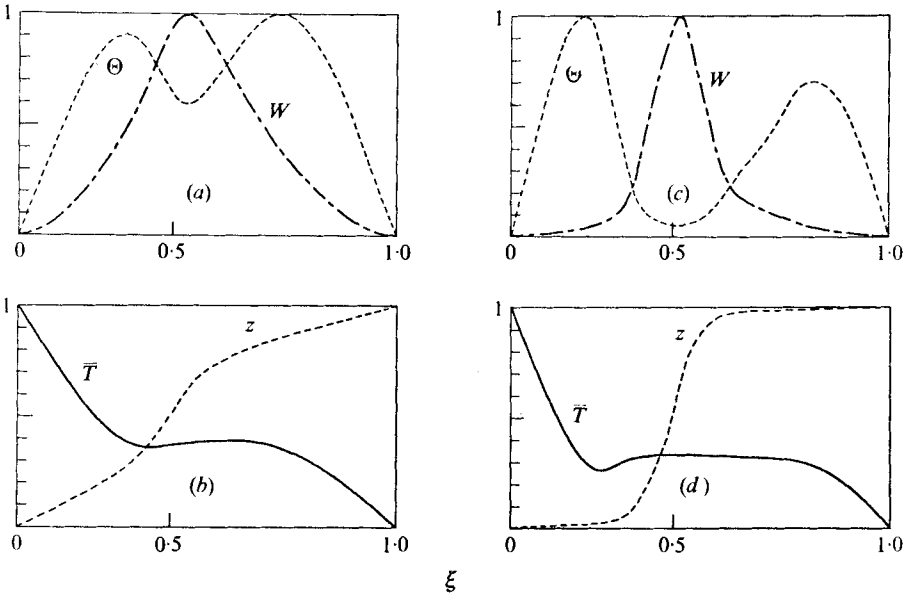

FIGURE 5. Variation of fields with increasing Rayleigh number R. Two steady solutions are shown: (*a*), (*b*) that at $R = 10^5$ and (*c*), (*d*) that at $R = 10^{10}$. Both solutions are at $a = 1{\cdot}0$, $C = 6^{-\frac{1}{2}}$ and $\sigma = 1{\cdot}0$. (*a*), (*c*) Amplitude functions $W(\xi)$ and $\Theta(\xi)$ of vertical velocity and of fluctuating temperature, plotted in units of their maximum values W_0 and Θ_0 and in terms of the stretched variable ξ. (*b*), (*d*) Mean temperature $\bar{T}(\xi)$ and inverse stretching function $z(\xi)$ (see appendix A). The solution at $R = 10^5$ is also displayed unstretched in figure 1. The extent of the stretching is suggested by δ_1 and δ_2, the distances of the lower and upper peaks of Θ from their nearest boundaries. (*a*), (*b*) $W_0 = 2{\cdot}68 \times 10^1$, $\Theta_0 = 0{\cdot}204$, $N = 3{\cdot}19$, $\delta_1 = 2{\cdot}57 \times 10^{-1}$, $\delta_2 = 1{\cdot}43 \times 10^{-1}$. (*c*), (*d*) $W_0 = 4{\cdot}52 \times 10^3$, $\Theta_0 = 0{\cdot}203$, $N = 4{\cdot}78 \times 10^1$, $\delta_1 = 1{\cdot}85 \times 10^{-2}$, $\delta_2 = 7{\cdot}05 \times 10^{-3}$.

for $C = 0$, and Murphy (1971*b*) has found some for $C \neq 0$; our agreement with these results is satisfactory.]

Figure 6 also depicts a solution for which W and Θ vanish in the interior. In all solutions of this type, we found that W and Θ vanish together. It can be shown that at such points $\partial^2 W/\partial z^2$ must vanish too. In principle, these overtone solutions could be compounded from fundamental solutions at appropriate (lower) Rayleigh numbers and wavenumbers, with suitable combinations of rigid and free boundary conditions. The example of a vertical overtone in figure 6 is essentially a combination of the solution at $R = \frac{1}{8} \times 10^{10}$, $a = 2.685$ with W, $\Theta > 0$ subject to rigid conditions at the lower boundary and free conditions at the upper one and the solution derived from it by the transformation (2.11). In this case the interior boundary layer in $\bar{T}$ is centred at $z = \frac{1}{2}$; had the boundary conditions at the top and bottom not been the same it would have occurred elsewhere. The interior boundary layers are all evenly spaced when the number of internal zeros of W exceeds one only if upper and lower boundaries are both free. It seems likely that the vertical overtone is unstable.

Detailed comparison of the R and a dependence of these numerical solutions with the predictions of our asymptotic analysis will be made in appendix B.

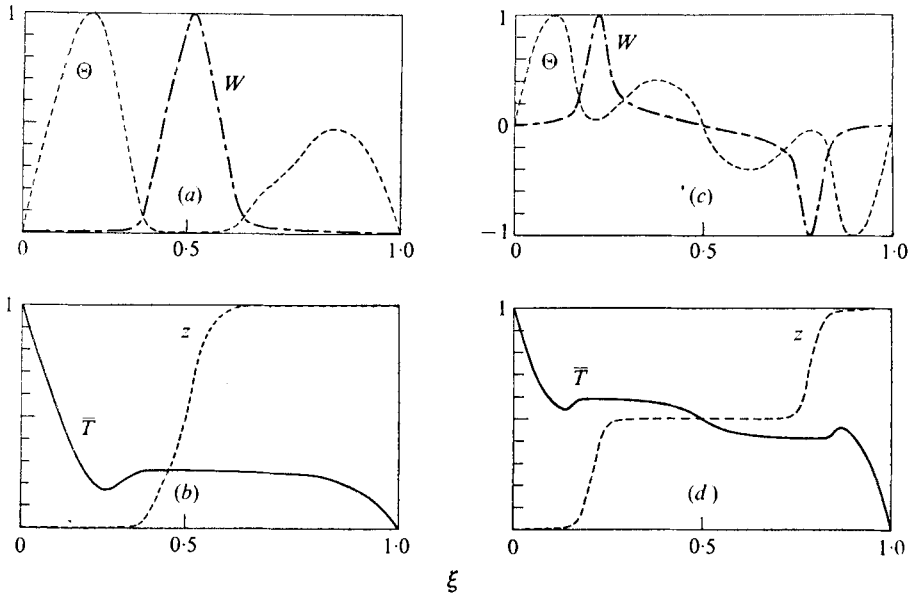

FIGURE 6. Similar to figure 5, again with $C = 6^{-\frac{1}{2}}$ and $\sigma = 1{\cdot}0$. (*a*), (*b*) Solution at $R = 10^{15}$ with $a = 1{\cdot}0$, which should be compared with the solutions in figure 5; here $W_0 = 5{\cdot}05 \times 10^5$, $\Theta_0 = 0{\cdot}226$, $N = 6{\cdot}08 \times 10^2$, $\delta_1 = 1{\cdot}63 \times 10^{-3}$ and $\delta_2 = 4{\cdot}26 \times 10^{-4}$. (*c*), (*d*) Fields of a vertical overtone solution at $R = 10^{10}$ with $a = 5{\cdot}37$; $W_0 = 5{\cdot}94 \times 10^3$, $\Theta_0 = 0{\cdot}125$, $N = 4{\cdot}96 \times 10^1$.

4.3. *Dependence on the interaction parameter C*

The dependence of N on C, though never very marked, is qualitatively different in different ranges of R and a. For $R = 10^6$, N is a monotonically decreasing function of C for fixed $a > a_m \approx 10$. For $R = 10^6$ and $a = 5$, N has a maximum with respect to C at $C \approx 0{\cdot}2$. Such details can be seen in figure 7.

As R increases above 10^6, a change in the C dependence occurs. For $R \simeq 10^{10}$ and $a \gtrsim a_m$, N is maximum at $C = 0{\cdot}2$, a value which is insensitive to R, and this is illustrated in figure 8 for $R = 10^{12}$ and $a = 800$. For very large values of R and $a \approx 1$, N again has a maximum with respect to C but at a much lower value, as the curves for $R = 10^{12}$ and 10^{20} in figure 8 show; the appearance of a distinct cliff near $C = 0$ with increasing R is clearly evident. Further, the filled circles indicate the values given by the asymptotic formula (3.1) for $C \neq 0$ evaluated at $R = 10^{20}$; the value for $C = 0$, based on (3.6), is shown by a filled triangle. Thus the asymptotic results display a behaviour resembling that of the numerical solutions.

These variations with C are minor and show that, for $C = O(1)$ and not too close to zero, the solutions are not sensitive to the choice of C. Though we can discern no clear pattern from these variations, they do indicate that it is not easy to tell in advance what the strengthening of nonlinearity will do to heat transport. We have (except at lower R) confined our calculations to $C \leqslant 6^{-\frac{1}{2}}$ since, as has been demonstrated by L. Baker (private communication), higher values cannot be attained by planforms f satisfying (2.3) in the entire x, y plane.

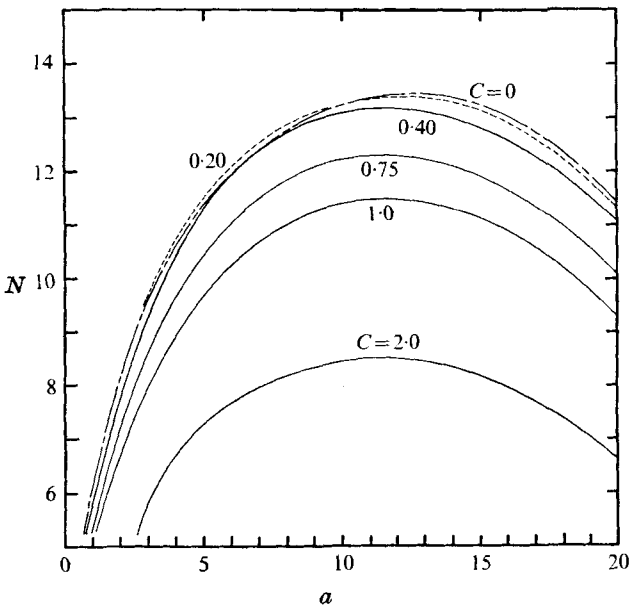

FIGURE 7. The variation of the Nusselt number N with the wavenumber a for various fixed values of C, all at $R = 10^6$ and $\sigma = 6{\cdot}8$ (water). Realizable planforms lie in the range $C = 0$ (for rolls) to $C = 6^{-\frac{1}{2}} = 0{\cdot}408$ (for hexagons); larger values of the interaction parameter C are included here to demonstrate the behaviour of the numerical solutions. At this moderate Rayleigh number, N is maximized by a $C = 0$ solution.

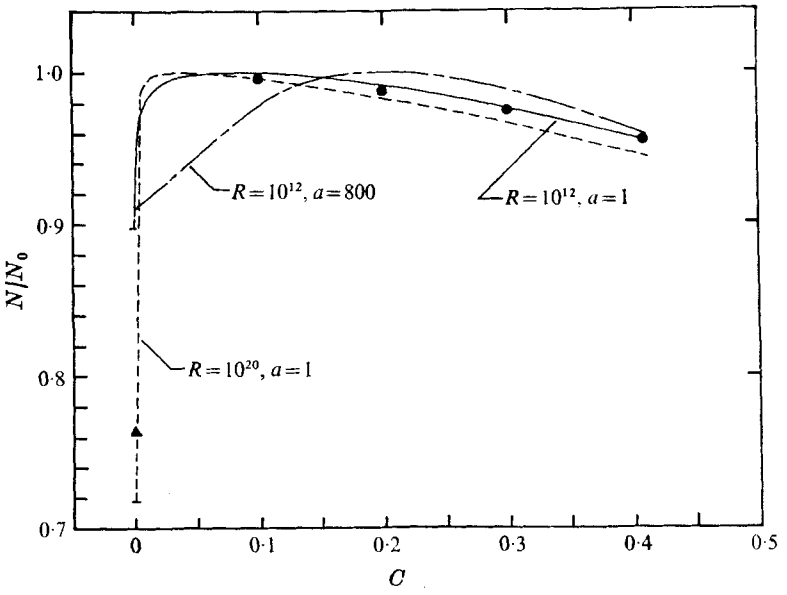

FIGURE 8. Variation of N/N_0 with C, where N_0 is the maximum of the Nusselt number with respect to C. All solutions are for $\sigma = 1$. The prominent cliffs in the solutions with $a = 1$ and $R = 10^{12}$ and 10^{20} (which have $N_0 = 140$ and 7820) are characteristic of all solutions at high R with a of order unity. The smoother behaviour of the solutions with $a = 800$ and $R = 10^{12}$ ($N_0 = 723$) is typical when $a \gtrsim a_m$. For comparison, asymptotic results are presented for $a = 1$ and $R = 10^{20}$. The circles were computed from (3.1) and the triangle from (3.6). The formula (3.1) increases monotonically as C decreases. The maximum in N occurs near $C = 0$, where (3.1) is not valid. The value $N_0 = 7830$ was chosen for the asymptotic points to give agreement with the numerical results at $C = 0{\cdot}1$.

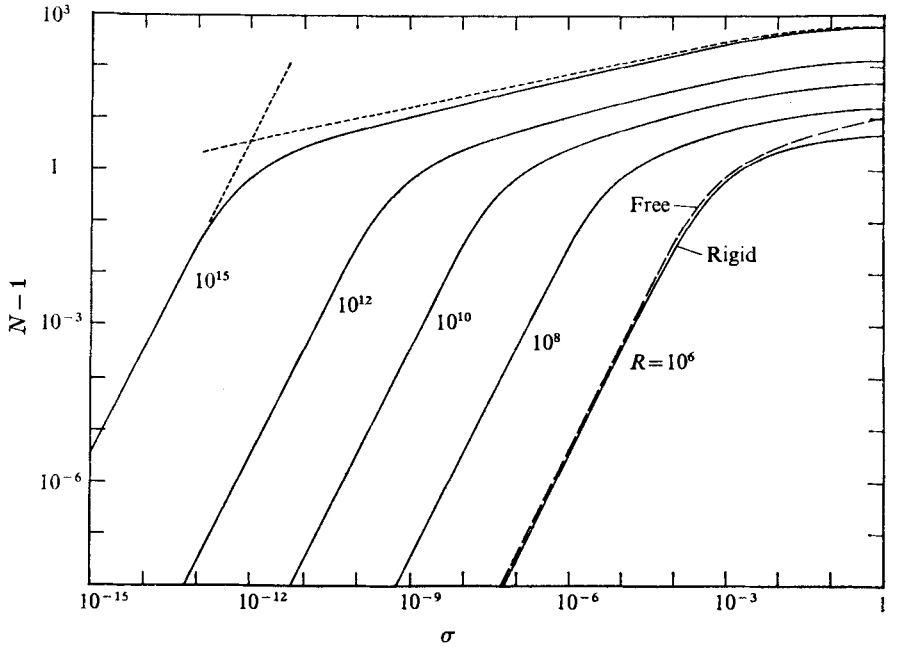

FIGURE 9. The heat transport $N-1$ as a function of the Prandtl number σ for several fixed values of R. In all these numerical solutions $a = 1$ and $C = 6^{-\frac{1}{2}}$. When $\sigma \lesssim 10^{-2}$, $N-1$ depends on σ and R only through the combination σR, and when $N-1 \lesssim 0{\cdot}1$ this dependence is approximately $N-1 \propto (\sigma R)^2$. The two curves at $R = 10^6$ demonstrate the effects of rigid and free boundary conditions: $N-1$ is almost independent of the boundary conditions at low σ in the quadratic regime, but the solutions differ noticeably when σ is of order unity. All other solutions satisfy the rigid conditions (2.9). The short-dashed curves represent the asymptotic formulae (3.1) and (3.8) for $R = 10^{15}$.

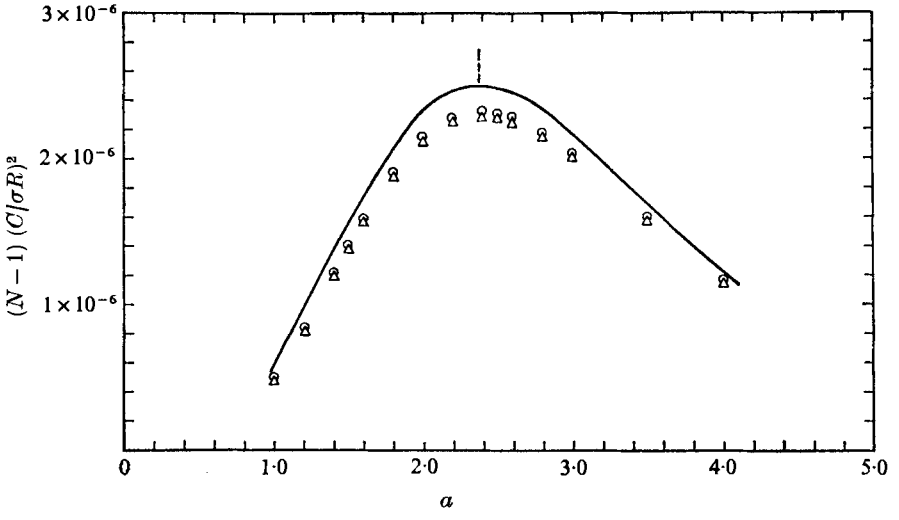

FIGURE 10. The variation of heat flux with horizontal wavenumber a at low Prandtl numbers σ. Asymptotic analysis (at high R and low σ) predicts that $(C/\sigma R)^2\,(N-1) \equiv \Lambda$ should be a function of a alone, and the continuous curve shows its behaviour. The discrete points plot the results of numerical solutions for hexagons at $R = 10^6$ with $\sigma = 10^{-5}$ (triangles) and $\sigma = 10^{-6}$ (circles). The dashed vertical line locates the wavenumber $a = 2{\cdot}370$, which maximizes Λ in the asymptotic solutions. The numerical results lie somewhat below the asymptotic limit because R is only 10^6. For $R \gtrsim 10^8$ the numerical and asymptotic results at $a = 1$ differ by less than 0·5%.

4.4. *Dependence on Prandtl number* σ

The most significant difference between the solutions with $C \neq 0$ and the mean-field solutions ($C = 0$) is the dependence on Prandtl number. For fixed R and a, N increases monotonically with σ for $C \neq 0$. The variation with σ is marked for $\sigma < 1$ but becomes very slight when $\sigma > 1$. As $\sigma \to \infty$, N approaches some constant value, as the asymptotic studies indicate. Numerical solutions for σ as large as 10^{15} confirm the behaviour at large σ and show that, for $\sigma \gtrsim 3$, N is within 1% of its value at $\sigma = \infty$.

The asymptotic analysis predicts that, when $\sigma \ll 1$, N is a function of σR and does not depend on σ and R separately, which means that the heat flux is independent of viscosity. This is borne out by the numerical solutions, some of which are depicted in figure 9 together with the asymptotic results for $R = 10^{15}$. Had these curves been plotted against σR instead of σ they would have been found to be coincident for $\sigma \ll 1$; the relative deviation from this common curve at moderate σ depends on σ but not on R, and is less than about 10% for $\sigma < 10^{-2}$.

For σ small and $\sigma R/C$ not large, so that $N - 1$ is small, the Nusselt number variation is given by (3.8). The coefficient Λ in (3.8) varies weakly with R, and approaches a limit as $R \to \infty$ which depends only on the wavenumber and agrees with the values derived from the matched asymptotic expansions to within the numerical accuracy. Thus it is evident that the form of the dependence of N on a in this limit becomes independent of σ, R and C at sufficiently large R. This is illustrated in figure 10 at $R = 10^6$ together with the limiting form (3.8) derived from the asymptotic analysis. The discrete numerical data presented lie below the limiting curve because they were computed at only a modest Rayleigh number. The value of the wavenumber a_m which maximizes N is insensitive to R.

5. Comparison with real convection

Having described the nature of the single-mode numerical solutions, we now assess their relevance to actual convection. In comparing the global properties of the solutions with laboratory experiments at given R and σ, we must specify a and C (and, strictly, the choice of vertical harmonic). Within the framework of the single-mode truncation, we have found no independent theoretical reason for preferring one horizontal wavenumber to another. In line with previous suggestions (e.g. Malkus 1954*b*) one might choose a to maximize N. This kind of device may ultimately prove to have merit, but at present there are not real grounds for adopting it. We turn instead to laboratory convection for guidance. Should an adequate procedure for the choice of a be suggested by the laboratory experiments, in the sense that at least the mean gross features of real convection are being reproduced by these solutions, we would then be encouraged to use similar procedures for predicting convective processes in parameter ranges beyond laboratory experience.

A difficulty with this approach is that the majority of experiments that

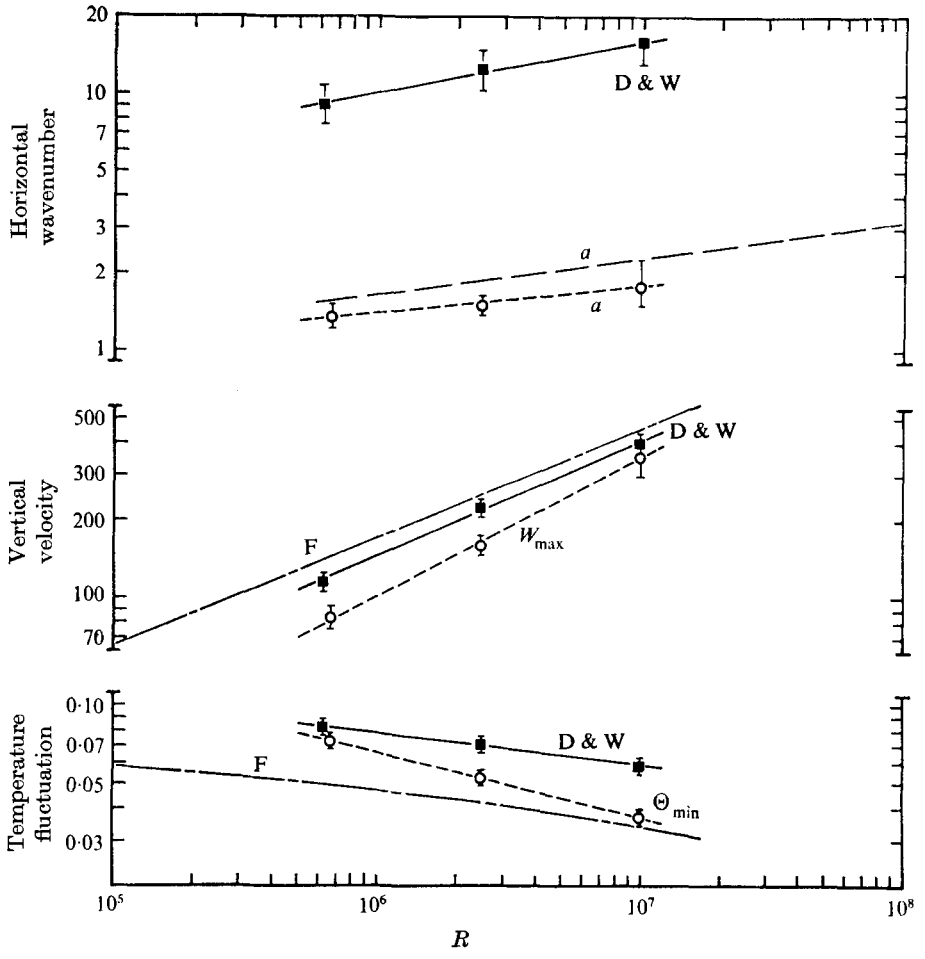

FIGURE 11. Comparison of single-mode results with laboratory experiments in air ($\sigma = 0{\cdot}70$). Solutions with $C = 6^{-\frac{1}{2}}$ were constructed to replicate the Nusselt numbers reported by Deardorff & Willis (1967) at three values of the Rayleigh number R; we chose solutions at the lower of the two possible wavenumbers a. The open circles denote the wavenumbers of these numerical solutions, along with W_{max} (the maximum of W with respect to z) and Θ_{min} (the minimum of Θ). Deardorff & Willis provide wavenumbers a below which 90% of the heat is transported, and these are shown as filled squares. Their values for the r.m.s. vertical velocity and fluctuating temperature at mid-layer are also so plotted (all labelled D & W). Similar velocity and temperature measurements by Fitzjarrald (1975) are shown by the broken curves (labelled F). The long-dashed curve denotes the wavenumbers a of our solutions used to replicate N in the experiments of Goldstein & Chu (1971), as indicated in figure 2.

measure N at large R are not concerned with the direct determination of scales of motion which we might associate with a. Some help is provided by the experiments which study how the cell shape, the wavenumber and the time dependence of the convection vary with R and σ (as recent examples, see Krishnamurti 1973; Busse & Whitehead 1974), but heat-flux data there is available only for moderate values of R. Of course, for $R \lesssim 2{\cdot}2 \times 10^4$ and $\sigma > 1$,

σ \ R	10^4	10^5	10^6	10^7	10^8	10^9	
0·025 (mercury)	1·57*	2·83	5·12*	—	—	—	Rossby (1969) $N = 0{\cdot}147\ R^{0.257}$
	—	—	5·10*	10·9	—	—	Globe & Dropkin (1959) $N = 0{\cdot}051\ R^{0.333}$
0·7 (air)	—	—	7·14	14·1	27·7	—	Goldstein & Chu (1971) $N = 0{\cdot}123\ R^{0.294}$
0·8 (helium)	2·28	4·35	8·28	15·8	30·1	57·3	Threlfall (1975) $N = 0{\cdot}173\ R^{0.280}$
6·8 (water)	2·41*	4·14	8·27	—	—	—	Rossby (1969) $N = 0{\cdot}131\ R^{0.300}$
	—	—	—	14·6*	28·7	56·4	Garon & Goldstein (1973) $N = 0{\cdot}130\ R^{0.293}$
	—	4·49*	8·52	16·2	30·7	—	Chu & Goldstein (1973) $N = 0{\cdot}183\ R^{0.278}$
18 (oil)	—	—	9·78	18·8	36·0	—	Somerscales & Gazda (1969) $N = 0{\cdot}196\ R^{0.283}$
200 (oil)	2·45	4·68	8·93	—	—	—	Rossby (1969) $N = 0{\cdot}184\ R^{0.281}$

Table 1. Nusselt numbers N reported from various laboratory experiments for selected Rayleigh numbers R and Prandtl numbers σ. These N were determined from the interpolation formulae provided by the experimenters; asterisks denote which entries for N lie slightly outside the range of R of a given experiment. The data are sparse, but there is a distinct decrease in N with decreasing σ.

a regime in which the observed motion is two-dimensional, the scales are fairly well determined (as summarized by Willis, Deardorff & Somerville 1972). But this does not take us into the regimes of higher R we need. In the face of the scarcity of such explicit information we shall simply pick those values of a that give the right N for the available measurements, and then inquire whether the remaining features of the solutions agree with the experimental results.

A primary group of convection experiments exists that provides the dependence of N upon R and σ. Rossby (1966, 1969) has contrasted his own extensive experiments using mercury ($\sigma = 0{\cdot}025$), water ($\sigma = 6{\cdot}8$) and a silicone oil ($\sigma = 200$) with those of previous workers including Schmidt & Saunders (1938), Malkus (1954*a*), Silverston (1958) and Globe & Dropkin (1959). Though these different experiments tend to have only limited overlap in both σ and R, Rossby points out the fair variation in the reported Nusselt numbers N. Other recent convection experiments that provide data on heat transport are those of Deardorff & Willis (1967), Goldstein & Chu (1971) and Fitzjarrald (1975) with air ($\sigma = 0{\cdot}7$), those of Threlfall (1975) with gaseous helium at low temperature ($\sigma = 0{\cdot}8$), those of Somerscales & Gazda (1969), Chu & Goldstein (1973) and Garon & Goldstein (1973) with water and those of Somerscales & Dropkin (1966)

with different silicone oils. Some of these experiments have obtained temperature profiles in addition to N, and a few have even measured velocity fields.

Table 1 displays the Nusselt numbers determined in some of the more recent experiments, presented for a selection of values of σ and R. Few of these investigations extend beyond $R = 10^8$, and the data are quite sparse at low σ. Still, this table illustrates two points. First, N appears to decrease with decreasing σ when R is fixed. This is certainly true of the series of experiments by Rossby, and his measurements of N correlate well with the results of others. Second, the heat-transport data are frequently presented for fixed σ in the form of simple power laws $N = \alpha R^{\beta}$. With the exception of Globe & Dropkin, all recent experimenters report values of the exponent β in the range 0·26–0·30; higher values have been reported also by earlier workers (e.g. Malkus 1954*a*).

As figure 2 (with $\sigma = 1$) suggests, the range of N available from the single-mode solutions readily encompasses the Nusselt numbers of Goldstein & Chu (1971) for air ($\sigma = 0{\cdot}7$) for $R = 10^6$–10^8. We have indicated with dashed lines the two values of a at each R for which the experimental and numerical convective transports are identical; the two choices of a lie on either side of a_m and increase with increasing R. Reference to the mean temperature field $\overline{T}(z)$ makes us prefer the smaller wavenumber since then the interior $\overline{T}$ is reasonably isothermal, in accord with the experiments. The fields displayed for $\sigma = 6{\cdot}8$ and $R = 10^6$ in figure 3 make this preference clear, for there the $a = 2$ and 24 solutions have identical N (7·9, as opposed to $N_m = 13{\cdot}1$ at $a = a_m = 12$), but only for the smaller a is $\overline{T}(z)$ somewhat like those in the corresponding Chu & Goldstein (1973) experiments with water. [Incidentally, these solutions in figure 3 had wavenumbers chosen, as round numbers, to obtain an N near the value of 8·3 of Rossby (1969) or the value of 8·5 of Chu & Goldstein (1973). Better estimates of a can be read from figure 7.] Thus, matching the Nusselt numbers and the general appearance of $\overline{T}(z)$ leads us to choose the lower of the two wavenumbers that reproduce N, at least in the moderate range of R attained in laboratory experiments.

The form of $\overline{T}(z)$ deserves comment. It has been suggested in the experimental papers that the mean temperature profile is asymmetric about the midplane, that a weak reverse gradient in $\overline{T}$ occurs in the nearly isothermal interior, that the interior value of $\overline{T}$ differs from $\frac{1}{2}$ and that bumps exist in $\overline{T}$ near the walls. Somerscales & Dropkin (1966) find all four features, Somerscales & Gazda (1969) report less pronounced asymmetries and weaker bumps, as do Chu & Goldstein (1973), while Rossby (1969) expresses concern that his $\overline{T}$ is not equal to $\frac{1}{2}$ at $z = \frac{1}{2}$. On the other hand, Goldstein & Chu (1971) report none of these features and Deardorff & Willis (1967) question experiments that reveal them. As our various $\overline{T}(z)$ profiles illustrate, the hexagon solutions are typically asymmetric and possess a bump, and these features are a natural consequence of three-dimensional cellular motion, with upward and downward velocities of unequal amplitude. However, our $\overline{T}$ bump is too pronounced, and the nearly isothermal interior values of our $\overline{T}$ lie outside the range of midplane values (roughly 0·45–0·55) reported from experiments. Clearly, just changing the sign of W and Θ in our hexagons reflects the asymmetries of the $\overline{T}$ profile about the midplane

while retaining the same N. It is tempting to conjecture that in some cells the flow may be upward in the middle and in some downward at a given instant, so that the globally averaged $\overline{T}$ might be approximated by averaging our two solutions, but that possibility cannot be dealt with in a single-mode treatment. Of the experimentally determined mean temperature profiles, the (time-averaged) profile of Thomas & Townsend (1957) compares favourably with the $\overline{T}$ in our figure 3(*a*); however we must treat this agreement with some caution, for the authors suggest that a single large-scale convection cell may have dominated the flow, and so their results may be atypical.

There is also some discussion on whether the experimental $\overline{T}$ profiles have a simple inverse-power-law dependence on the distance z from the wall, as predicted by some theories (Priestley, 1954 chap. 4; Malkus 1954*b*; Kraichnan 1962). Although some authors (e.g. Somerscales & Dropkin 1966; Goldstein & Chu 1971; Chu & Goldstein 1973) have managed to fit such a simple formula to their data, it appears that the functional dependence is really more complicated, as has been pointed out by Somerscales & Gazda (1969), who found better agreement with a theory due to Howard (1966). We find that our $\overline{T}$ in the boundary layers, when measured in units of the mean temperature drop across the appropriate boundary layer, deviates from the experimental profiles by no more than the difference between the experiments. The absolute values are not good, however, because our interior values of $\overline{T}$ are incorrect.

We come now to some subtler consequences of choosing the wavenumber a to duplicate the experimental N. The work of Deardorff & Willis (1967) is particularly relevant, for they made simultaneous velocity and temperature measurements of convection in air, undertook spatial spectral analysis, and computed various correlations among the data. More recently, Fitzjarrald (1975) conducted a similar investigation, with the advantage that he could vary the aspect ratio of the apparatus. We have constructed solutions with $\sigma = 0{\cdot}70$ which duplicate the Nusselt numbers inferred by Deardorff & Willis at their three distinct values of R. The wavenumbers a of such solutions (using the lower of the two possible a's) are shown in the compound figure 11 as open circles; each such a has a range of uncertainty (indicated by vertical bars) which reflects the uncertainty in the experimental values of N. Now what bearing do these a's have on experimental measures of horizontal scale?

Deardorff & Willis and Fitzjarrald present time-averaged (arithmetic mean) Fourier spectra of the spatial fluctuations in velocity and temperature measured along a horizontal line. The spectra at different Rayleigh numbers are too dissimilar for peaks to be unambiguously associated. However, the data of Deardorff & Willis suggest that there are some scales which increase with R and others which decrease. Fitzjarrald looked also at the W, Θ cospectra before time averaging and selected the wavelengths of the three highest peaks. This was done for many records and a distribution function for these wavelengths was constructed. It was found that, when the aspect ratio of the apparatus was large, the peaks in this distribution function moved to larger wavelengths as R increased. However, when the aspect ratio of the apparatus was reduced in one direction and the spectra measured longitudinally, the reverse trend was found.

It is difficult to draw general conclusions from these analyses, especially since the available data are sparse. What is clear is that there are several important horizontal scales of motion evident in the spectra, and we are attempting to model the flow with just one. Perhaps the most relevant experimental measures with which to compare this are the values obtained by Deardorff & Willis of the scale in the covariance of W and Θ above which 90 % of the heat is transported in the interior ($z = 0{\cdot}5$). It might be expected that the wavenumbers corresponding to these length scales are representative of, though they would underestimate, the eddies that dominate the transport of heat. In representing heat transfer by a single mode, we associate the preferred a with the energy-transporting scales of motion. We display these experimental wavenumbers as filled squares in figure 11. These experimental measures of horizontal scale are rather different in magnitude from those of our N-duplicating solutions. What agreement exists is just that the various wavenumbers increase with R in approximately the same manner.

The data of Deardorff & Willis and Fitzjarrald also permit us to compare our fluctuating vertical-velocity and temperature amplitudes with the corresponding experimental r.m.s. amplitudes. Plotted in figure 11 are $W_{\max}$ and $\Theta_{\min}$, the maximum and minimum with respect to z of W and Θ in our solutions, and the maxima and minima of the analogous experimental profiles of the r.m.s. fluctuations. The slopes of the curves with R are similar. The discrepancies between theory and observation are of the same order as the differences between the results of the two sets of experiments. Further, the product of our $W_{\max}$ and $\Theta_{\min}$ (which is effectively N in the interior) is consistently lower than the products of the corresponding r.m.s. fluctuations. This arises because perfect correlation between velocity and temperature fluctuations is built into the single-mode representation, whereas the real flows do not achieve this: Deardorff & Willis find correlations of order 0·5, Fitzjarrald's are of order 0·8.

The z dependence of the r.m.s. velocity and temperature fluctuations is not in agreement with our W and Θ. Garon & Goldstein (1973) find that the vertical velocity varies as the one-third power of distance from the boundary, contrary to our predictions in either boundary layer (cf. (4.17) and (4.18), and figure 1 of I). Although the shapes of the experimental temperature fluctuations measured by Rossby (1966) and Somerscales & Gazda (1969) superficially resemble Θ, the maxima of Θ are too large by a factor of 2.

It would be unreasonable to expect a description based on only a single horizontal length scale to reproduce faithfully the statistics of a turbulent flow. Nevertheless, we do find that, if we choose the value of a that reproduces the correct Nusselt number, this value at least varies with R in a similar fashion to the mean wavenumber of the 'eddies' carrying the heat. Furthermore, the velocity and temperature fluctuations we predict with that a are not far removed from the corresponding actual fluctuations. The experimental data available for such comparisons are very limited, and at the admission of some of the authors not wholly reliable, so that we cannot make a clear statement of the success of the present effort. Even if it transpires that our truncated modal description of convection is wholly inadequate, more sophisticated theories that

will no doubt appear in the future can be adequately tested only if a greater body of data becomes available.

Finally we should examine how N varies with σ, and what is implied about a. As table 1 shows, the experimental data at low σ are few; likewise the grid of numerical solutions presented here is rather coarse in σ. But such comparisons as are possible are comforting to us. For fixed R the heat transport reported in experiments appears to decrease systematically with σ, as does that in our hexagons for fixed (R, a) in figure 9. For example, at $R = 10^6$ the experimental $N-1$ decreases from 6·1 to 4·1 as σ falls from 0·70 to 0·025, a reduction of about 30 %; the numerical $N-1$, for the arbitrary a of 1 in figure 9, is decreased by a similar percentage, from 4·7 to 3·1. This suggests that the 'preferred' a is relatively insensitive to σ, at least over this narrow range of σ.

6. Conclusion

The upshot of these calculations is that the single-mode results, with judicious choices of a and C, can be made to reproduce the observed heat transport and some aspects of the behaviour of the temperature profiles. This is not a great tribute to their validity since other aspects of the flow are not well modelled and the experiments are not of wide scope. In fact, we have already pointed out a failure of the single-mode results at high values of R: that solutions exist with temperatures which are in places outside the range defined by the boundary conditions. This is a serious flaw and arises from having too crude a representation of the advection terms. In an intensely turbulent flow of a Boussinesq fluid with constant transport coefficients it is reasonable to expect the mean temperature of the isothermal interior to lie midway between the boundary values. However we do not achieve this, since our single-mode solutions with $C \neq 0$ are highly asymmetric when σR is large. A more suitable representation of the flow might be provided by a two-mode solution constructed from two similar planforms with the same wavenumber, and representing, for example, hexagons with motion upwards and downwards in the middle respectively. We have obtained some results with such two-mode hexagons for $R \leqslant 10^7$ which show that solutions exist where the upward and the downward motions are of comparable amplitude, and $\bar{T}$ in the isothermal interior assumes a value of about 0·5. The heat transport is very close to that predicted by a single-mode solution at the same wavenumber.

Another source of concern about the single-mode equations is the behaviour of N with R as $R \to \infty$. As we discussed in I, the steepest variation that can be achieved asymptotically by the single-mode solutions is $N \sim R^{\frac{3}{10}}(\ln R)^{\frac{1}{5}}$, which falls somewhat short of the widely believed, but experimentally unverified, $R^{\frac{1}{3}}$ variation or the even more rapid variation predicted by Kraichnan (1962). It does appear likely, however, that we can reproduce the $R^{\frac{1}{3}}$ behaviour by using a representation with a sequence of modes interacting only through the mean temperature field (reported by Spiegel 1971), each mode in the sequence having a wavelength of the same scale as the boundary layer produced by the one before it. Such a sequence was also used by Chan (1971) in his heat-flux

maximization study at infinite σ. If the modes interact directly through the fluctuation advection terms, it may be that the asymptotic dependence is steeper. However, for the present we seem able to reproduce the existing experimental results for R up to about 10^{12} with the single-mode approximation since $N \propto R^{0.28}$ appears to be the best current representation of the experiments, with a spread in the reported values of the exponent of about ± 0.02.

The fashion in which we must choose a and C to predict the heat flux has not been significantly elucidated by the comparison with experiments. It is clear that for large R the motions are three-dimensional and this suggests that $C \neq 0$. Moreover for C not close to zero N is not sensitive to C. By its definition, $C = O(1)$, and the general appearance of high Rayleigh number convection suggests that $C = 6^{-\frac{1}{2}}$ (hexagons) is a reasonable choice.

The selection of the horizontal wavenumber a is more difficult since it depends significantly on R and possibly on σ. The rough indications from the comparisons we have made in figures 2 and 11 are that a is close to but somewhat less than the value that maximizes N. Since the maximizing value varies like $R^{\frac{1}{4}}$ we suppose that the optimal choice of a does also, but this awaits verification. As to the dependence of the preferred a on σ we have no real guidance from the experiments.

It is interesting that similar difficulties are found in direct numerical simulations of convection. Most of that work is confined to two-dimensional studies (as discussed by Lipps & Somerville 1971; Moore & Weiss 1973), except at very modest R. These studies effectively impose a wavenumber for the rolls by the placement of end walls, though L. Bauer & E. L. Reiss (private communication) have been attempting to minimize this by using very large aspect ratios. Here too one does not know how to choose a, except by reference to experiments. Experimental values of a are available at large σ for $R \lesssim 2{\cdot}2 \times 10^4$, where the motion occurs as rolls, and when these are used in the simulations the heat transport is in good agreement with the experiments (Willis *et al.* 1972). But otherwise the choice of a is not apparent.

Perhaps the most important feature of the single-mode solutions is their Prandtl number dependence when $C \neq 0$. In particular, we predict a decrease in the Nusselt number N as σ decreases below unity, in the manner shown in figure 9. Kraichnan (1962) had previously concluded from a mixing-length approach that N should decrease with σ. Similar results have been obtained at very low σ (Ledoux, Schwarzschild & Spiegel 1961; Spiegel 1962). However, such reductions in heat transport with decreasing σ have not been seen in the two-dimensional numerical simulations (see Veronis 1966; Moore & Weiss 1973), though there is some evidence for it in the three-dimensional work of Veltishchev & Želnin (1975). Further, this behaviour of N is at variance with the results of Jones, Moore & Weiss (1975), who studied axisymmetric convection in an upright circular cylinder with stress-free boundaries. This geometry permitted them to consider three-dimensional motions while still dealing with only two spatial independent variables. They found that N in fact increased slightly with decreasing σ at moderate R.

The source of the discrepancy appears to be the profound change in the flow

field revealed by the two-dimensional computations as σ decreases. At low σ the flow is such that the vorticity is constant on streamlines, as is the case for rolls. This has the effect of annihilating the nonlinear advection term in the momentum equation and allowing the velocities to build up to very high values, much as in a fly-wheel. These fly-wheel solutions have a horizontal structure very different from that of a single-mode planform f satisfying (3.1) for this axisymmetric problem (for which $C = 0{\cdot}18$). Although it is likely that fly-wheel solutions are unstable to three-dimensional disturbances and hence might not be realized in practice, they do provide fair warning of flows with special horizontal structures that behave quite differently at low σ from the ones we have considered.

It is perhaps unusual in a classical subject such as this to find that one cannot test theories (if they may be so called) because of insufficient data. But the experiments are difficult, especially at high R, though Threlfall (1975) has recently achieved $R \simeq 10^{11}$ using helium at a low temperature. His results are limited to heat-flux measurements and the aspect ratios are rather small. But the means for measuring fluid velocities and temperatures in such conditions are available and aspect ratios can be improved. We strongly urge experimenters to extend this work, and also to undertake studies at low Prandtl numbers, available with liquid metals, to resolve the issue concerning fly-wheel solutions.

One reason for hesitation to enter the high R regime experimentally may be the risk of encountering wide variations in T and hence noticeable variations in viscosity and conductivity. Such effects are normally excluded from the simplest theories and there may be reluctance to lose contact with the theory. However, the inclusion of variation of the transport coefficients in the calculations is not an essential difficulty (see appendix C). Similar remarks apply to deviations from what are normally considered ideal boundary conditions. The ultimate problems to be solved contain these difficulties and they should not deter the experimental work that is urgently needed.

The needs we refer to are of those who must estimate convective transfer in attempting to deal with fluid-dynamical problems in geophysics or astrophysics. This comes up in so many problems that extreme measures must be taken. The present inability to solve the relevant full equations, or at least to find the right kind of solution, in the appropriate parameter ranges has forced many workers to renounce the attempt and proceed in any way that seems feasible. We are perhaps part of the way into this camp, but would at least like to keep things in hand by experimental tests whenever possible. We believe that in this respect the procedure we have explored may have advantages over the more usual mixing-length theory. On the other hand, the amount of work required to realize any such advantage is far greater than in mixing-length theory, and we freely admit that our case is not yet a strong one. What we have exhibited here, however, is needed as an introduction to the higher approximations to be presented later, which show time dependence and other peculiarities of real convection.

The major part of the numerical studies were carried out in New York at the Goddard Institute for Space Studies (GISS). During much of this effort J.T.

was at GISS and in the Department of Mathematics, New York University, and D.O.G. was at GISS and at the Courant Institute of Mathematical Sciences, New York University; J.T. and D.O.G. held NAS-NRC fellowships while at GISS. We are also grateful for the financial support to the National Science Foundation, most recently under NSF Grants MPS 75-05660 and DES 74-14439, and to the National Aeronautics and Space Administration under NASA Contract NGL 06-003-057.

Appendix A. Numerical methods

This appendix outlines the numerical procedures used in integrating the system of single-mode equations (2.4)–(2.6), subject to the boundary conditions (2.8) and (2.9) or (2.10). The same techniques may also be used when dealing with the more complicated multi-mode equations given in I. These parabolic systems of nonlinear partial differential equations, with time t and the vertical spatial co-ordinate z as the independent variables, are solved by finite differences.

When R or a is large, or σ is small, the solutions tend to have boundary layers. To resolve their structure adequately a non-uniform spatial mesh in z is helpful. We have therefore introduced a stretched independent variable $\xi(z)$ in [0, 1] with respect to which the M grid points (M is typically about 300) are evenly spaced; ξ is chosen such that boundary-layer regions occupy a suitable proportion of the domain of ξ. The stretched variable ξ is a monotonic function of the original independent variable z. When only simple boundary layers in the neighbourhood of $z = 0$ and $z = 1$ are encountered, explicit functional forms for the mapping $\xi(z)$ can be chosen, with scaling parameters that are determined from approximate solutions of the basic equations. This method becomes laborious when nested boundary layers of different thicknesses are encountered, when for example R is large and σ is small, or when internal boundary layers associated with vertical harmonics arise. We therefore devised a more direct method for determining the stretched variable $\xi(z)$, based on minimizing estimates of the truncation error introduced by differencing. One such error estimate is the integral of the sum of the squared curvatures with respect to ξ of all the variables in the basic problem, including the original independent variable z; the Euler equations determining the minimum, with their natural boundary conditions and an integral constraint defining the range of ξ, are solved in conjunction with the basic system of differential equations. Details of stretching techniques, based on either explicit functions or various functionals of the solutions, have been presented elsewhere (Gough, Spiegel & Toomre 1975*b*).

Difference equations were constructed by representing all spatial derivatives by centred differences of second-order accuracy and representing time derivatives in a way that gave consistent emphasis to all terms in the equations, whether linear or nonlinear, at each time level. Implicit time schemes are necessary when dealing with highly stretched spatial grids because the diffusive stability criterion ($\Delta t \leqslant 0\ [(\Delta z_{\min})^2]$) would otherwise impose prohibitively small time integration steps Δt. Hybrid multi-level time schemes that treat only the

linear terms implicitly, to relax the diffusive criterion, and compute the nonlinear terms explicitly introduce phase differences between the fluctuating advective terms and the linear terms which can result in spurious oscillations (whose properties depend on the grid spacing).

The nonlinear difference equations that result from our implicit time schemes are solved at each time step by a Newton–Raphson iteration (cf. Henrici 1962, p. 366), leading to the repeated inversion of a large $(M \times M)$ block bidiagonal or tridiagonal matrix. This procedure can be made definitive by noting that (2.4)–(2.6), plus any additional equations resulting from a functional form for the stretching, can be written as a set of J equations of the form

$$\sum_{\beta=1}^{J} \Lambda_{\alpha\beta} \frac{\partial u_\beta}{\partial t} = \mathscr{N}_\alpha(u_\gamma), \quad \alpha, \gamma = 1,\ldots, J, \tag{A 1}$$

where $\mathscr{N}_\alpha$ is a differential operator in ξ and Λ is a constant matrix all of whose elements are either 0 or 1. The solution vector $\mathbf{u}(\xi, t)$ can be represented on a finite-difference grid of M spatial points at each time level n by the discrete variables $u_{i\alpha}^n$, where the independent variables are similarly $\xi = \xi_i^n$, $t = t^n$, $i = 1,\ldots, M$, $n \geqslant 0$. The finite-difference form of (4.1) then becomes

$$\sum_{\beta=1}^{J} \Lambda_{\alpha\beta} \frac{u_{\beta i}^n - u_{\beta i}^{n-1}}{\Delta t^n} = q\mathscr{N}_{\alpha i}(u_{\gamma j}^n) + (q-1)\mathscr{N}_{\alpha i}(u_{\gamma j}^{n-1}), \tag{A 2}$$

where the time step $\Delta t^n = t^n - t^{n-1}$ and $\mathscr{N}_{\alpha i}$ is the difference operator obtained from $\mathscr{N}_\alpha$ by replacing spatial derivatives by centred differences of second-order accuracy. The diffusive criterion is relaxed for implicit time schemes with the parameter q in the range $[\frac{1}{2}, 1]$.

To advance the solution in time from the $(n-1)$th to the nth time level, we solve a system of nonlinear algebraic equations for $u_{\alpha i}^n$ in terms of $u_{\alpha i}^{n-1}$, which may be formally written as

$$\mathscr{F}_{\alpha i}(u_{\beta j}^n, u_{\gamma k}^{n-1}) = 0, \quad \alpha, \beta, \gamma = 1, \ldots J, \quad i, j, k = 1, \ldots, M. \tag{A 3}$$

If $n = 1$, $u_{\alpha i}^{n-1}$ represents the initial conditions, and the boundary conditions (2.8) and (2.9) or (2.10) at $\xi = 0, 1$ (or at $z = 0, 1$) determine $\mathscr{F}_{\alpha 1}$ and $\mathscr{F}_{\alpha M}$. The nonlinear equations (A 3) are solved readily by Newton–Raphson iteration, in which the Lth iterate of $u_{\alpha i}^u$ is written as

$$u_{\alpha i}^{n,L} = u_{\alpha i}^{n,L-1} + \delta u_{\alpha i}^{n,L}, \tag{A 4}$$

and it is assumed that $|\delta u_{\alpha i}^{n,L}| \ll |u_{\alpha i}^{n,L-1}|$. Substituting (A 4) into (A 3) and expanding the resulting equation to first order in $\delta u_{\alpha i}^{n,L}$ yields the linear system

$$\mathscr{F}_{\alpha i}(u_{\beta l}^{n,L-1}, u_{\gamma k}^{n-1}) + \sum_{j=1}^{M} \sum_{\nu=1}^{J} \frac{\partial \mathscr{F}_{\alpha i}(u_{\beta j}^{n,L-1}, u_{\gamma k}^{n-1})}{\partial u_{\nu j}^{n,L-1}} \delta u_{\nu j}^{n,L} = 0, \; i, k, l = 1, \ldots, M, \quad \alpha, \beta, \gamma = 1, \ldots, J. \tag{A 5}$$

For integrations of the time-dependent equations the iterations were started by setting $u_{\alpha i}^{n,1} = u_{\alpha i}^{n-1}$, and were terminated when for some specified number E

$$\sum_{i=1}^{M} \sum_{\alpha=1}^{J} |\delta u_{\alpha i}^{n,L}| \Big/ \sum_{i=1}^{M} \sum_{\alpha=1}^{J} |u_{\alpha i}^{n,L}| < E. \tag{A 6}$$

The rate of convergence of this Newton–Raphson iteration is quadratic, and it was usually possible to obtain solutions with $E = 10^{-14}$.

Several different decompositions of the form (A 1) were used, the $\mathscr{N}_\alpha$ being either all first-order or all second-order operators (with $J = 8$ or 4 for the single-mode equations when additional stretching equations were not involved). The coefficient matrix of $u_{vj}^{n_j L}$ in (A 5) which must be inverted is then either block bidiagonal or block tridiagonal and order $M \times M$, with blocks of order $J \times J$. Some care must be taken in performing the inversion of these large matrices to ensure that numerical error is kept small.

The steady version of the single-mode equations (2.4)–(2.6) was solved in the same way. In cases where an eigenvalue is present, either because the mesh-stretching procedure requires one or when the integrated form (2.7) of the energy equation is used in place of (2.6), simultaneous iteration of the solution vectors and the eigenvalues can be performed with a small modification to the above procedure, as described by Baker, Moore & Spiegel (1971). The integral constraint

$$\int_0^1 (N - W\Theta)\, dz = 1,$$

which replaces the boundary conditions (2.8) when (2.7) is used, can be treated similarly.

Sequences of steady solutions were computed by varying one of the parameters defining the problem, for example R. Given two neighbouring solutions, we projected linearly to a new value of R to obtain an initial estimate for the Newton–Raphson iteration of a third solution. In view of the almost self-similar nature of the solutions, we found it sufficient merely to project the mesh-stretching function and the amplitudes of the solutions, while retaining the functional forms of the fields in ξ space. This projection is not necessary to obtain convergence, but it does permit one to take larger jumps in the parameter which is being varied. For example, it is possible to project half a decade or more in R over the whole range from about 10^3 to 10^{25} when $a = 1$, $\sigma = 1$ and $C = 6^{-\frac{1}{2}}$. Smaller increments were usually taken in surveys of the other parameters, so that the curves presented in this paper could be adequately resolved. Fully converged solutions are obtained after only six to eight iterations in this quadratically convergent scheme, requiring of the order of 4 s (with $M = 300$) of IBM 360/95 machine time. The results presented in this paper are based upon several thousand distinct solutions surveying the R, a, σ, C parameter space. Several independently written programs produced indistinguishable results.

Appendix B. Comparison between numerical and asymptotic solutions

To test the accuracy of the numerical solutions we compare them with the asymptotic results for $R \to \infty$. Estimates of truncation errors are rarely precise. Often we used the steady form of the mean energy equation (2.6) instead of its integral, then constructed $N(z) \equiv -d\overline{T}/dz + W\Theta$ and tested it for constancy: for $R = 10^6$ ($a = 1$, $C = 6^{-\frac{1}{2}}$, $\sigma = 1$) the relative variation in N was less than 10^{-4}, for $R < 10^{22}$ it could be kept below $\frac{1}{2}\%$ if 600 mesh points were used, and for our solution at $R = 10^{25}$ it was about 4%. However, constancy of N pro-

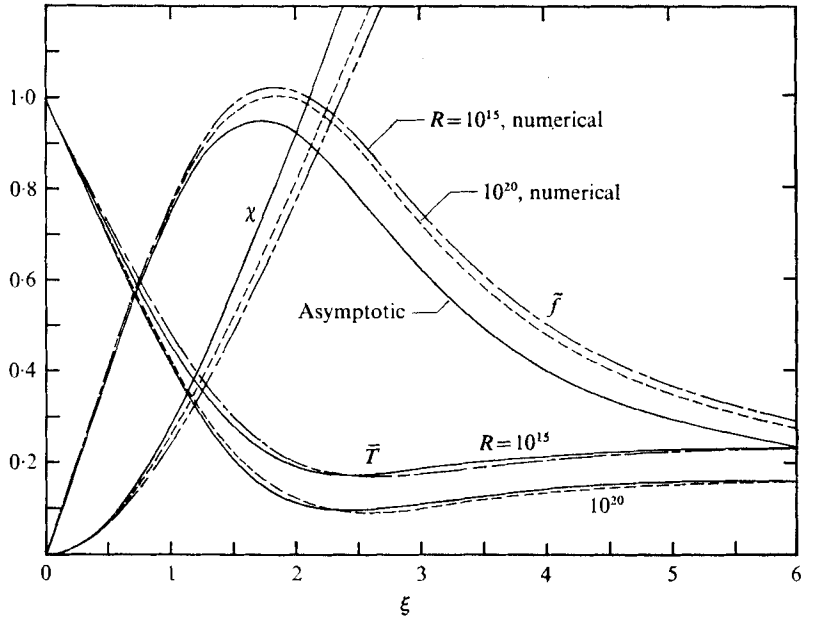

FIGURE 12. The numerical velocity and temperature fields in the lower boundary layer for $R = 10^{15}$ and 10^{20} are compared with the results of the asymptotic analysis (as $R \to \infty$). Here $a = 1$, $C = 6^{-\frac{1}{2}}$, $\sigma = 1$. The vertical-velocity amplitude function W has been scaled to become χ, the fluctuating temperature Θ to become $\tilde{f}$, while $\bar{T}$ remains the usual mean temperature field; all are shown as functions of the lower-boundary-layer variable ξ, in the manner of figure 1 in I. The agreement between the numerical and asymptotic solutions improves with increasing Rayleigh number.

vides only a rather insensitive measure of the reliability of our numerical schemes. Without a comparison with the asymptotic solutions in their common regions of validity, we would have less confidence in the numerical solutions.

The most obvious comparisons to make are between the values of N calculated by the two methods. For R in the range 10^{10}–10^{25}, $a = 1$, $\sigma = 1$ and $C = 6^{-\frac{1}{2}}$, the numerical and asymptotic solutions agree to within 3 %. Comparisons are also made in figures 2 and 9, which show the dependence of N on a and σ. The value of k' was not calculated in I by solving the upper-boundary-layer equation. It was rather evaluated here from the numerical solutions with $C = 6^{-\frac{1}{2}}$, $a = 1$ and R in the range 10^{15}–10^{25} using (3.4), which gave $k' = 1{\cdot}73$ to within 1 % at $\sigma = 1$. Comparisons of solutions with $C = 0$, and with $C = 6^{-\frac{1}{2}}$ subject to free boundary conditions, give similar agreement.

The Nusselt number is a relatively insensitive measure of the accuracy of the solutions, and a more detailed comparison between the asymptotic and the numerical results is desirable. We also compared the dependences on R of $W_{\max}$, the maximum of $W(z)$, and $\Theta_{\max_1}$ and $\Theta_{\max_2}$, the maxima of $\Theta(z)$ in the lower and upper boundary layers respectively (for $C \neq 0$). The dependence of $W_{\max}$ on R is hardly distinguishable from $R^{\frac{2}{5}} (\ln R)^{\frac{1}{15}}$ for R above about 10^{10} (we could not compare absolute magnitudes because we have not integrated the asymptotic interior equation). However the slope of $\Theta_{\max_2}$ attains only 90 % of

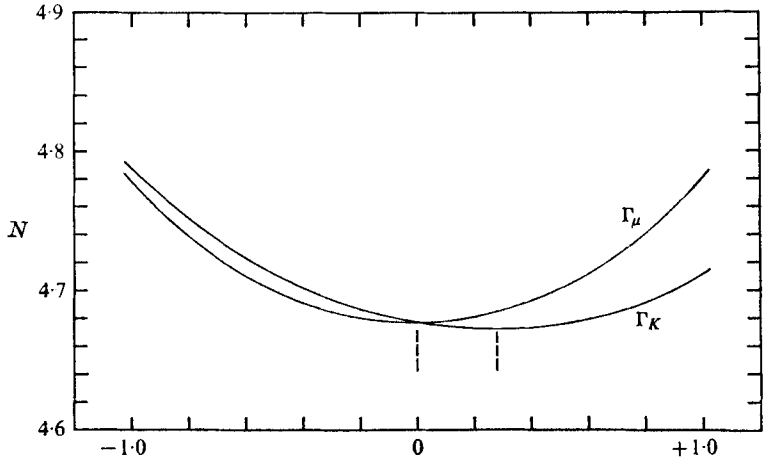

FIGURE 13. Variation of the Nusselt number N with the degree of temperature dependence of the shear viscosity μ and the thermal conductivity K, as in (C 1) and (C 2). The curve labelled Γ_μ has μ varying and K constant, i.e. $\Gamma_K = 0$, and shows N plotted against Γ_μ. The curve marked Γ_K has K varying and μ constant, i.e. $\Gamma_\mu = 0$. All solutions are for $R = 10^6$, $a = 1$, $C = 6^{-\frac{1}{3}}$ and $\sigma = 1$.

its asymptotic value by $R = 10^{20}$. At this value of R, $\Theta_{\max_1}$ is not yet constant, since the approach to the asymptotic regime is very slow. The approach of the thickness of the lower boundary layer to $\delta_1 \simeq 3\,(R \ln R)^{-\frac{1}{3}}$ is also slow. The constant ratio $\Theta_{\max_2}/\overline{T}_i = 0{\cdot}415$ is achieved to within 1 % by about $R = 10^{12}$, and the asymptotic relation between the thickness of the upper and lower boundary layers (measured as the distance from the Θ maxima to the nearest boundary), namely $\delta_1 \sim 1{\cdot}5\,\delta_2^{\frac{5}{3}}(\ln \delta_2^{-1})^{-\frac{1}{3}}$, is satisfied to within 1 % for $R > 10^5$.

The spatial structure of the velocity and temperature fields at large R is given in figure 12. Here are shown $(C/\sigma)^{\frac{1}{3}}N^{-1}W$, $(\sigma/C)^{\frac{1}{3}}\Theta$ and $-N^{-1}\,\mathrm{d}\overline{T}/dz$ in the lower boundary layer at various values of R, and the corresponding asymptotic boundary-layer solutions χ, f and $\overline{T}$ of I. They are plotted with respect to a uniformly stretched independent variable $\xi = (\sigma/C)^{\frac{1}{3}}Nz$, the same co-ordinate as is used in figure 1 of I.

Some comparison between the numerical and asymptotic dependences of N upon a and C at large R is provided in figures 2 and 8. Figure 10 shows that the a dependence of $N-1$ at low σ and moderate R is qualitatively similar to the form predicted by the asymptotic analysis. The quadratic σ dependence of $N-1$ at low σ is accurately reproduced at all R (see figure 9) but the constant of proportionality deviates by more than 1 % from its asymptotic value unless $R \gtrsim 10^9$.

Appendix C. Variable transport coefficients

The entire study up to this point has been devoted to representing the motion of an ideal fluid whose molecular transport coefficients are constant. It is not difficult, however, to extend our treatment to allow for variable physical properties of the fluid.

For illustrative purposes we present here some solutions in which either the shear viscosity μ or the thermal conductivity K has been allowed to vary with mean temperature according to the law

$$\mu \propto 1+(\bar{T}-\tfrac{1}{2})\Gamma_\mu \tag{C 1}$$

or

$$K \propto 1+(\bar{T}-\tfrac{1}{2})\Gamma_K, \tag{C 2}$$

where the gradients Γ_μ and Γ_K are constant. The dependence upon the temperature fluctuations was neglected, because the variation in Θ is less than that in $\bar{T}$, but with a little more labour (2.4)–(2.6) could have been modified to include it.

Figure 13 illustrates the behaviour of the Nusselt number as either Γ_μ or Γ_K varies. The Rayleigh number R and Prandtl number σ are defined using the values of μ and K at $\bar{T} = \frac{1}{2}$. The solutions have W, $\Theta > 0$; solutions with negative velocity and temperature amplitudes can be derived from them by making the transformation (2.11) and changing the signs of Γ_μ and Γ_K. Note that when K varies in the simple way (C 2) the heat transport in the conduction state is independent of Γ_K, so there is no ambiguity in the definition of N.

REFERENCES

Baker, N. H., Moore, D. W. & Spiegel, E. A. 1971 Aperiodic behavior of a non-linear oscillator. *Quart. J. Mech. Appl. Math.* **24**, 391–422.

Busse, F. H. & Whitehead, J. A. 1974 Oscillatory and collective instabilities in large Prandtl number convection. *J. Fluid Mech.* **66**, 67–80.

Chan, S. K. 1971 Infinite Prandtl number turbulent convection. *Studies in Appl. Math.* **50**, 13–49.

Chandrasekhar, S. 1961 *Hydrodynamic and Hydromagnetic Stability*. Oxford: Clarendon Press.

Chu, T. Y. & Goldstein, R. J. 1973 Turbulent convection in a horizontal layer of water. *J. Fluid Mech.* **60**, 141–159.

Deardorff, J. W. & Willis, G. E. 1967 Investigation of turbulent thermal convection between horizontal plates. *J. Fluid Mech.* **28**, 675–704.

Fitzjarrald, D. E. 1975 An experimental study of turbulent convection in air. *J. Fluid Mech.* **73**, 693–719.

Garon, A. M. & Goldstein, R. J. 1973 Velocity and heat transfer measurements in thermal convection. *Phys. Fluids*, **16**, 1818–1825.

Globe, S. & Dropkin, D. 1959 Natural-convection heat transfer in liquids confined by two horizontal plates and heated from below. *J. Heat Transfer*, **81**, 24–28.

Goldstein, R. J. & Chu, T. Y. 1971 Thermal convection in a horizontal layer of air. *Prog. Heat Mass Transfer*, **2**, 55–75.

Gough, D. O., Spiegel, E. A. & Toomre, J. 1975*a* Modal equations for cellular convection. *J. Fluid Mech.* **68**, 695–719.

Gough, D. O., Spiegel, E. A. & Toomre, J. 1975*b* Highly stretched meshes as functionals of solutions. *Proc. 4th Int. Conf. Numer. Meth. Fluid Mech.* (ed. R. D. Richtmyer), pp. 191–196. *Lecture Notes in Physics*, vol. **35**. Springer.

Henrici, P. 1962 *Discrete Variable Methods in Ordinary Differential Equations*. Wiley.

Herring, J. R. 1963 Investigations of problems in thermal convection. *J. Atmos. Sci.* **20**, 325–338.

Herring, J. R. 1964 Investigation of problems in thermal convection: rigid boundaries. *J. Atmos. Sci.* **21**, 277–290.

Howard, L. N. 1966 Convection at high Rayleigh number. *Proc. 11th Int. Cong. Appl. Mech.* (ed. H. Görtler), pp. 1109–1115. Springer.

JONES, C. A., MOORE, D. R. & WEISS, N. O. 1975 Axisymmetric convection in a cylinder. *J. Fluid Mech.* **73**, 353–388.

KRAICHNAN, R. J. 1962 Mixing-length analysis of turbulent thermal convection at arbitrary Prandtl numbers. *Phys. Fluids*, **5**, 1374–1389.

KRISHNAMURTI, R. 1973 Some further studies on the transition to turbulent convection. *J. Fluid Mech.* **60**, 285–303.

LEDOUX, P., SCHWARZSCHILD, M. & SPIEGEL, E. A. 1961 On the spectrum of turbulent convection. *Astrophys. J.* **133**, 184–197.

LIPPS, F. B. & SOMERVILLE, R. C. J. 1971 Dynamics of variable wavelength in finite-amplitude Bénard convection. *Phys. Fluids*, **14**, 759–765.

MALKUS, W. V. R. 1954*a* Discrete transitions in turbulent convection. *Proc. Roy. Soc.* A**225**, 185–195.

MALKUS, W. V. R. 1954*b* The heat transport and spectrum of thermal turbulence. *Proc. Roy. Soc.* A**225**, 196–212.

MOORE, D. R. & WEISS, N. O. 1973 Two-dimensional Rayleigh–Bénard convection. *J. Fluid Mech.* **58**, 289–312.

MURPHY, J. O. 1971*a* Nonlinear thermal convection with free boundaries. *Aust. J. Phys.* **24**, 587–592.

MURPHY, J. O. 1971*b* Non-linear convection with hexagonal planform. *Proc. Astron. Soc. Austr.* **2**, 53–54.

PRIESTLEY, C. H. B. 1954 *Turbulent Transfer in the Lower Atmosphere.* University of Chicago Press.

ROBERTS, P. H. 1966 On non-linear Bénard convection. *Non-Equilibrium Thermodynamics, Variational Techniques, and Stability* (ed. R. Donnelly, R. Hermann & I. Prigogine), pp. 125–162. University of Chicago Press.

ROSSBY, H. T. 1966 An experimental study of Bénard convection with and without rotation. Ph.D. thesis, Massachusetts Institute of Technology.

ROSSBY, H. T. 1969 A study of Bénard convection with and without rotation. *J. Fluid Mech.* **36**, 309–335.

SCHMIDT, R. J. & SAUNDERS, O. A. 1938 On the motion of a fluid heated from below. *Proc. Roy. Soc.* A**165**, 216–228.

SILVESTON, P. L. 1958 Wärmedurchgang in Waagerechten Flüssigkeitsschichten. *Forsch. Ing. Wes.* **24**, 59–69.

SOMERSCALES, E. F. C. & DROPKIN, D. 1966 Experimental investigation of the temperature distribution in a horizontal layer of fluid heated from below. *Int. J. Heat Mass Transfer*, **9**, 1189–1204.

SOMERSCALES, E. F. C. & GAZDA, I. W. 1969 Thermal convection in high Prandtl number liquids at high Rayleigh numbers. *Int. J. Heat Mass Transfer*, **12**, 1491–1511.

SPIEGEL, E. A. 1962 Thermal turbulence at very small Prandtl number. *J. Geophys. Res.* **67**, 3063–3070.

SPIEGEL, E. A. 1971 Convection in stars. I. Basic Boussinesq convection. *Ann. Rev. Astron. Astrophys.* **9**, 323–352.

STEWARTSON, K. 1966 Asymptotic theory in limit $R \to \infty$. *Non-Equilibrium Thermodynamics, Variational Techniques, and Stability* (ed. R. Donnelly, R. Hermann & I. Prigogine), pp. 158–162. University of Chicago Press.

THOMAS, D. B. & TOWNSEND, A. A. 1957 Turbulent convection over a heated horizontal surface. *J. Fluid Mech.* **2**, 473–492.

THRELFALL, D. C. 1975 Free convection in low-temperature gaseous helium. *J. Fluid Mech.* **67**, 17–28.

VELTISHCHEV, N. F. & ŽELNIN, A. A. 1975 Numerical simulation of cellular convection in air. *J. Fluid Mech.* **68**, 353–368.

VERONIS, G. 1966 Large-amplitude Bénard convection. *J. Fluid Mech.* **26**, 49–68.

WILLIS, G. E., DEARDORFF, J. W. & SOMERVILLE, R. C. J. 1972 Roll-diameter dependence in Rayleigh convection and its effect upon the heat flux. *J. Fluid Mech.* **54**, 351–367.